Measuring Lyman Continuum Emission from High Redshift Galaxies

Master Thesis
by
Niels-Erik Stenby Kofod

Supervisor:
Associate professor
Johan P. U. Fynbo

Copenhagen University
Niels Bohr Institute
Dark Cosmology Centre

December 23, 2009

Dark Cosmology Centre

Abstract

The subject of this master thesis is measurement of how much ionizing radiation is escaping from galaxies at high redshift. In this context, what is meant by ionizing radiation, is radiation that is capable of ionizing hydrogen. That is, radiation with an energy of 13.6 eV or more. When we observe the intergalactic medium, we find that it is highly ionized. Today, it is not clear where the ionizing radiation is coming from. We know for a fact, that this kind of radiation is escaping from the centers of active galaxies, but it is generally concluded that the active galaxies are to few in numbers to be able to produce enough ionizing radiation to keep the intergalactic medium ionized. Consequently, it is debated whether star forming galaxies plays an important role, maybe even dominating the ionization of the intergalactic medium. It has also been debated wether decaying dark matter could play the role of delivering ionizing photons to the intergalactic radiation field.
The purpose of my thesis is to analyze existing data from the Very Large Telescope and determine how much ionizing radiation is escaping from the star-forming galaxies in my sample. My sample consist of 18 Lyman-α emitters. An important part of my work on this thesis has been dedicated to give a thorough introduction of this subject and what is already known from the literature on this topic.

NEC FASCES
NEC OPES
SOLA ARTIS
SCEPTRA PERENNANT
Not power, nor wealth,
only the reign
of art and science
shall persist
Tycho Brahe 1546 - 1601

Acknowledgements

First I would like to thank Johan P. U. Fynbo for being a great and patient supervisor and for the valuable help and guidance. I would also like to thank Ikuru Iwata for giving me the opportunity to work with an important part of the observational data, that this thesis is based on.

Finally, I would like to thank my family and friends for the help and support during the years. A special thanks to my Mom, Birthe, who have always stood by me.

And Lene, thank you for getting me through the last couple of month.

Contents

Preface ix

1 Introduction 1
- 1.1 Big Bang 1
- 1.2 The Formation of Structure 2
- 1.3 The Cosmic Microwave Background 5
  - 1.3.1 The Temperature Anisotropy 5
  - 1.3.2 Polarization of the Cosmic Microwave Background 7
- 1.4 The Formation of The First Stars 7
- 1.5 Reionization and The End of The Dark Ages 9
  - 1.5.1 Lyman-α Absorption Clouds 10
  - 1.5.2 The Gunn-Peterson Test 12
  - 1.5.3 The Proximity Effect 12
- 1.6 Decaying Dark Matter Particles 14
- 1.7 Finding High Redshift Galaxies 14
  - 1.7.1 The Lyman Break Technique 15
- 1.8 Lyman-α emission as a Probe for Early Star Formation 15
  - 1.8.1 Finding LAE using the narrow-band technique 17
- 1.9 Measuring Lyman-Continuum Emission from High Redshift Galaxies 17
  - 1.9.1 Previous Results 18

2 Observations 23
- 2.1 The VLT 23
  - 2.1.1 CCD setup before 2007 23
  - 2.1.2 New CCD setup 24
- 2.2 The field of BRI 1202-0725 25

3 Data Calibration 29
- 3.1 Bias and Flat-Fielding 29
  - 3.1.1 Calibration of Science Images 30
- 3.2 Combining Science Frames 30
- 3.3 Magnitude zero point from spectrophotometric standard stars 32

4 Photometry and Escape Fractions **39**
4.0.1 Photometric measurements 39
4.1 Magnitudes Calculation 40
4.2 Specific Flux and Luminosity Density 42
4.3 The Escape Fraction of Ionizing Photons 61
4.3.1 The Intrinsic Luminosity Density Ratio 63
4.3.2 The Intergalactic Medium Opacity 63
4.3.3 Results 63

5 Summary and Discussion **65**
5.1 Summary 65
5.2 Discussion 66

A Charged-Coupled Device **69**

B Tables **73**
B.1 74
B.2 75

Preface

The intergalactic medium in our present Universe is highly ionized. We also know that before the first stars started shining, the Universe was generally very neutral. Most astronomers are convinced that these first stars started the reionization of the Universe. However, the first very luminous stars lived very shortly, so at some time, other sources of ionizing radiation most have taken over. We are convinced that quasars play an important role in the ionization of the intergalactic medium at redshift up to $z \sim 3$. Beyond this redshift, we do not know for certain what sources dominated the reionization of of the Universe after the first stars had died out. A strong candidate for producing ionizing photons are star-forming galaxies such as Lyman Break Galaxies and Lyman-α emitters. However, only a few detections of ionizing Lyman continuum emission from these galaxies have been reported so far. This means that we are still very far from understanding the role of these star-forming galaxies in connection to the reionization of the intergalactic medium.

In this master-thesis I will search for Lyman continuum emission from a sample of 18 Lyman-α emitters and try to estimate the escape fraction of ionizing UV photon relative to the number of non-ionizing UV photons.

Niels-Erik Stenby Kofod
Københavns Universitet
December 23, 2009

Chapter 1

Introduction

This thesis is based on analysis of data of one of the largest telescopes in the world, the VLT. However, before we start on the data analysis, I would like put my work into a broader context. In this introductory chapter, I will get into some of the details concerning the ionization of the Universe, and the role that star-forming galaxies might play in this matter. Before we get their, I would like to start with the beginning, and since most astronomers are convinced that the Universe started in a Big Bang, I will also start their.

1.1 Big Bang

Our model for the Universe tells us that it started at least 13 billion years ago in a hot Big Bang and has expanded and cooled since then. When the Universe was one tenth of a second old it had a temperature of 3×10^{10} K and neutrons and protons were in equilibrium with each other, meaning they where created and destroyed at the same rate through the processes:

$$n + \nu_e \leftrightarrow p + e^- \tag{1.1}$$
$$n + e^+ \leftrightarrow p + \overline{\nu}_e \tag{1.2}$$

The electrons and positrons were continually created out of the background radiation which originated from the annihilation of matter and antimatter at an even earlier time. As long as the temperature was sufficiently high, so that the thermal energy, k_BT, was higher than the difference in rest energy of the neutron and proton, there were nearly the same number of neutrons and protons present in the early Universe. If protons and neutrons had gone on being in equilibrium with each other, the number of neutrons compered too the number of protons would have continued dropping during the cooling of the Universe, but when the Universe was 1 second old the neutrinos froze out, meaning that reaction (1.1) and (1.2) did not any longer take place in equilibrium. This happened because the cross-sections for weak interactions have the temperature dependence $\sigma_w \propto T^2$ and when the temperature dropped, σ_w became very small when the Universe was more than 1 second old. At "neutrino freeze out" the ratio between neutrons and protons was $1 : 5 = 20\%$, so when the baryons started to interact there was a upper limit for how much helium could come out of the Big Bang nucleosynthesis (BBN).

The first essential step in the BBN was the fusion of protons and neutrons to form deuterium nucleus:

$$p + n \leftrightarrow D + \gamma \tag{1.3}$$

where the binding energy is carried away by a gamma ray. Even though the BBN starts a few seconds after the big bang it takes a couple of minutes before half of the neutrons in the Universe are tied up in deuterium, because the temperature is too high at the start of BBN for the process to be efficient. When deuterium had formed, many possible nuclear reactions were available. For instance, a deuterium nucleus can fuse with a proton to form ^{3}He or it can fuse with a neutron to form tritium, which can be regarded as stable during the brief time that BBN lasted. The products ^{3}He and ^{3}H can then fuse into ^{4}He. Another possibility for deuterium nuclei is to fuse with each other and form ^{4}He directly, or the outcome of fusion between deuterium nuclei could be a ^{3}He or a tritium nucleus, which again can fuse into ^{4}He. The point is that all these fusion process lead to the creation of ^{4}He.

We might expect that the BBN would continue and crate still heavier elements, but the building blocks nature had were primarily neutrons and hydrogen and helium nuclei which have mass numbers 1 or 4. The logical step would then be for nature to create elements with mass number 5 or 8, e.g. by fusion process like:

$$\begin{aligned} {}^4\mathrm{He} + n &\rightarrow {}^5\mathrm{He} \\ {}^4\mathrm{He} + p &\rightarrow {}^5\mathrm{Li} \\ {}^4\mathrm{He} +^4 \mathrm{He} &\rightarrow {}^8\mathrm{Be}, \end{aligned}$$

but in nature there are no stable nuclei with mass number 5 or 8 so this will not work. However, it was possible for nature to create small amounts of ^{6}Li and ^{7}Li by fusing ^{4}He with D and ^{4}He with ^3H. All in all, the BBN was over in approximately 10 minutes, and the result was a universe where the baryonic component was divided into $\sim 75\%$ hydrogen, $\sim 25\%$ helium and a very small amount of lithium.

1.2 The Formation of Structure

Now that we have a universe where the baryonic component is dominated by hydrogen and helium it is relevant to ask, how do we get from this to the stars and galaxies we se in our Universe today. The first step we have to take in order to answer this questions, is the formation of structures and the role of dark matter.

We can consider the Universe as being homogeneous and isotropic only on scales larger than 100 Mpc across. On smaller scales however, the Universe consist of superclusters and voids which have typical sizes of 50 Mpc across. These large scale structures give the Universe a "bubbly" or "foamy" look as can be seen in figure 1.1. The figure shows the spatial distribution of galaxies observed in two strips across the

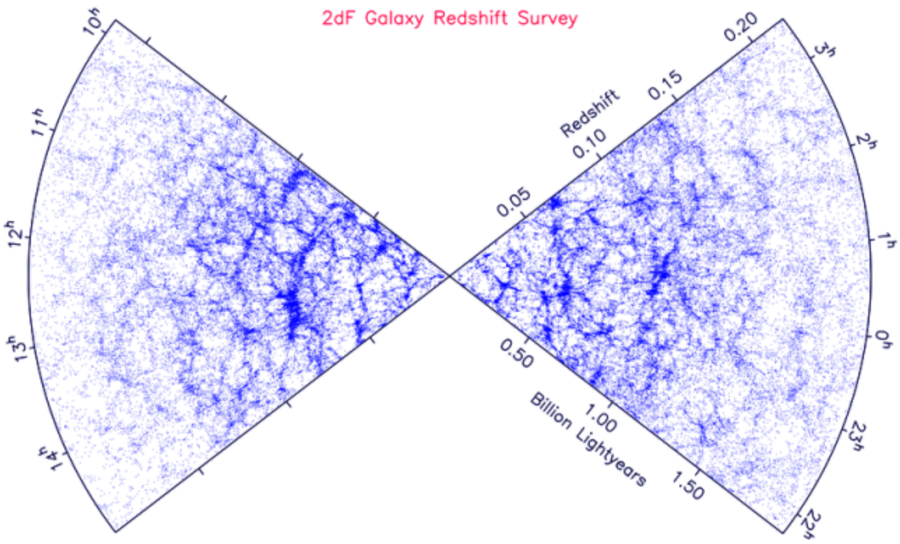

Figure 1.1: The distribution of galaxies in space as mapped out by the 2dF Galaxy Redshift Survey. Each tiny dot represent one or more galaxy.

sky. The galaxies make up structures which can be described as filaments or walls. When we observe the cosmic microwave background radiation (CMB), we see that small density fluctuations where present at a time when the Universe was less than 400.000 years old. It is then relevant to ask how these small density fluctuations grew to the structures we see in our present age of the Universe. The CMB was created at a time when matter dominated the cosmic density parameter Ω and the fluctuations evolved through this period of matter-domination by a mechanism called gravitational instability. To understand this better we start by introducing the energy density $\varepsilon(\vec{r},t)$, of some component of the Universe. This is a function of position and time, see *e.g.* Ryden (2003). From this we have at a given time t, the spatially averaged energy density:

$$\bar{\varepsilon}(t) = \frac{1}{V}\int_V \varepsilon(\vec{r},t)d^3r. \tag{1.4}$$

The volume V has to be bigger than the largest structure in the universe. We can also define a dimensionless density fluctuation as

$$\delta(\vec{r},t) \equiv \frac{\varepsilon(\vec{r},t) - \bar{\varepsilon}(t)}{\bar{\varepsilon}(t)} \tag{1.5}$$

and using this definition, δ becomes negative in underdense regions and positive in overdense regions.

If we want to study how large scale structures evolve we will have to know how small density fluctuations grows under the influence of gravity. As long as the condition $|\delta| \ll 1$ is satisfied we can use linear perturbation theory and we find that under the assumption of a static Universe with no pressure, gravity tends to make small density perturbations grow exponentially. It we introduce pressure we find that only overdense regions larger than the Jeans Length λ_J will be able to collapse under its own gravity. The Jeans Length depend on the sound speed of the medium because a change in the pressure will move through the medium with this velocity. Overdense regions that are smaller than λ_J, will then have time to maintain hydrostatic equilibrium and thereby resist gravitational collapse.

If we abandon the static universe and instead introduce the more realistic concept of an expanding Universe and general relativity we find that the density fluctuation grows according to Ryden (2003):

$$\ddot{\delta} + 2H\dot{\delta} - \frac{2}{3}\Omega_m H^2 \delta = 0 \tag{1.6}$$

where Ω_m is the matter component of the density parameter and the term $2H\dot{\delta}$ is the so-called Hubble friction, that will slow down the growth of density perturbations in an expanding universe. The point is, that because the timescale of the expansion and the timescale of collapse under self-gravity are similar, the global expansion will try to make the overdense regions less dense with time. The consequence of Ω_m interring into equation (1.6), is that during epochs when the Universe is not dominated by matter, the amplitude of the perturbations will only grow slowly. This means that in the first ~ 50.000 years after big bang when the universe was dominated by radiation, the density fluctuation in the dark matter grew only at a logarithmic rate. The baryonic matter was of cause still couplet to the radiation field and did not take part in the collapse of dark matter, before after the decoupling took place ~ 380.000 years after Big Bang. The fact that the baryonic content of the universe did not decouple from the radiation field until some time into the epoch of matter-domination means that after decoupling the baryonic component could collapse onto an already existing dark matter structure. Because baryons and electrons can interact with electromagnetic radiation it was able to cool and therefor condense even further and fall through the dark matter structure where galaxy and star formation began to take place.

When the amplitude of a overdense region reaches $\delta \sim 1$ its evolution can no longer be treated using linear perturbation theory, so studies of galaxy and star formation are usually done by numerical computer simulations.

Basically dark matter is divided into two different kinds, cold dark matter and hot dark matter. Cold dark matter consists of particles, which had velocities $v \ll c$ at the time they decouple from the other components of the universe. Hot dark matter consists of particles that had velocities $v \approx c$ when they decoupled, and remained relativistic until the time of radiation-matter equality, ~ 50.000 years after big bang. The idea is that if most of the dark matter in the universe was in the form of hot dark matter, e.g. neutrinos, any small scale density fluctuations in the matter component would be wiped out because of the high velocities. When the hot dark matter became nonrelativistic, there would be no density fluctuations on scales smaller than superclusters. This means that superclusters would have been the first structures to form in the Universe. However, this is not what we see when we look at observations. In fact, what we see is that superclusters are just starting to form in our present universe, whereas structures like galaxies seems to have started to form beyond redshift $z \sim 6$. The conclusion must be that the dark matter component of the universe consist primarily of cold dark matter. However, smaller amounts of hot dark matter, like neutrinos that do have mass, seems also to exist.

Before we go on to the formation of the first stars, I will discuss the cosmic microwave background in more detail, because it tells us about the ionization state of the Universe.

1.3 The Cosmic Microwave Background

Let us take a closer look at the cosmic microwave background (CMB) and what it tells us about the ionization history of the Universe. Most people with just a slight interest in astronomy know that our Universe is filed with a microwave radiation of cosmic origin. The CMB was created when the universe cooled and the radiation decoupled from the baryonic component of the Universe. In according to our model for the Universe, this happened approximately 380.000 years after Big Bang and constitute one of the important events in the history of the Universe. The result of this decoupling of baryons and photons was that neutral atoms could form for the first time in the Universe and what we today call the CMB is the last scattering surface, generated when the photons last was being scattered on the depleting free electrons. Since all the CMB photons did not make the last scatter at the same time, the last scattering surface is actually more like a last scattering layer were some photons have been traveling for a longer time to reach us than others. When the photons decoupled from the baryons and electrons, the epoch called The Dark Ages started. It is called so because light (photons) and the baryonic component plus electrons did not interact during this period in time. Nor were the first stars formed yet, so no source of optical light existed and the consequence today is, that we do not receive any optical light from this epoch.

The CMB is one of most important tools in cosmology, because it reveals the Universe's initial conditions. It also gives us information of the universe's structure and dynamics from the time of the CMB's origin to today. A CMB photon, measured using *e.g.* a space based CMB observatory, is encoded with the condition of the Universe along its ~ 13 billion years journey. This means that the CMB acts as a backlight, illuminating the transition from bulk-neutrality to complete reionization of the intergalactic medium (IGM). Since the discovery of the CMB in 1965 we have made increasingly more detailed observations of the fluctuations in the CMB. It turns out that we can use both the temperature anisotropy and the polarization of the CMB to help reconstruct the details of the End of Reionization (EoR)(Fan et al., 2006).

1.3.1 The Temperature Anisotropy

Observing the CMB reveals that the spectrum is very close to that of an ideal black-body. When we subtract the distortion from the motion of the observatory/sattelite

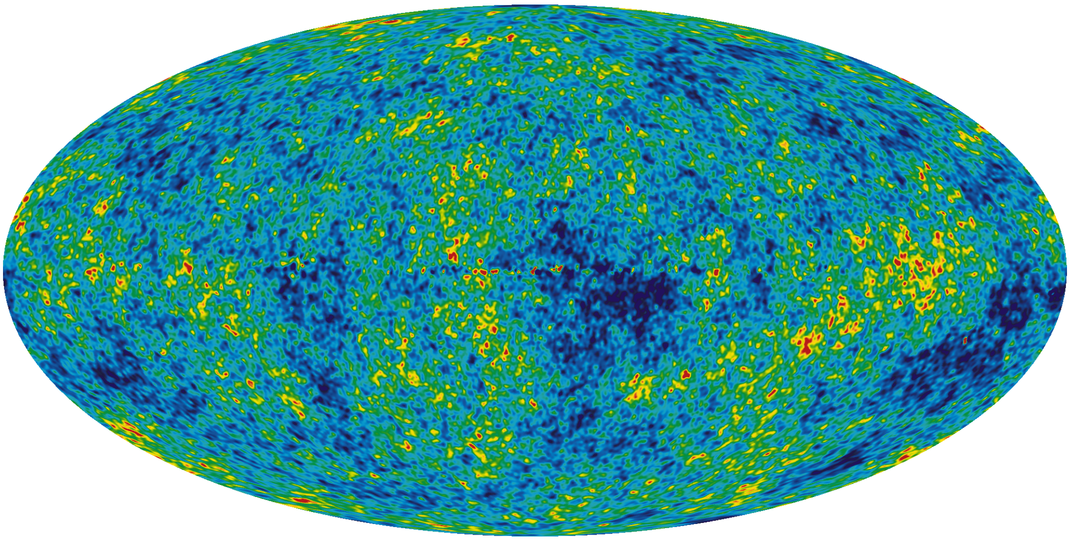

Figure 1.2: The cosmic microwave temperature fluctuations from the 5-year WMAP data seen over the full sky. The contribution from dipole distortion and the Galaxy has been subtracted. The average temperature is 2.725 K. Red regions are warmer and blue regions are colder by about 0.0002 K. The figure is taken from the WMAP home page: http://map.gsfc.nasa.gov/news/index.html#microwavesky.

and the contribution from the Galaxy we see that the mean temperature, averaging over the hole sky is $\langle T \rangle = 2.725$ K. The temperature fluctuate only with about 0.0002 K, from this mean temperature. An image of the temperature fluctuations observed by the Wilkinson Microwave Anisotropy Probe (WMAP) can be seen in figure 1.2. The angular resolution of the WMAP data is down to 15 arcminutes depending on the instrument channel used. It can be shown that two points on the last scattering surface that is separated with an angel $\theta_H = 2.1°$ (Longair, 2008) could not have been in causal contact at the time when the CMB was generated. As mentioned in section 1.2 at the time of last scattering the dark matter formed an underlaying structure that the baryionic component could collapse onto. Since the energy density of the dark matter dominated over both the radiation and baryionic energy density, at the time of last scattering it means the gravitational potential did vary spatially. If we consider a CMB photon that happened to be at a local minimum of the potential at the time of last scattering. This photon will lose energy climbing out of the potential well, and consequently is redshifted. On the other hand, photons that happens to be at a potential maximum when the Universe became transparent gains energy as they moves out of, or "down" from the maximum, and are thus slightly blueshifted relative to the average CMB photons, when they reaches us. When we look at the temperature map figure 1.2, the cold spots corresponds to regions of higher density and hot spots corresponds to regions of lower density at the time recombination. The pattern of cold and hot spots can be interpret as sound waves in the fluid that were present at the time of recombination. The study of these primordial sound waves can tell us about the average densities of matter and dark energy in the fluid, as well as the value of thee Hubble constant and age of the Universe.

1.3.2 Polarization of the Cosmic Microwave Background

The WMAP did also measure the polarization of the CMB. The CMB is being polarized due to Thomson scattering of the radiation by free electrons. It is because the free electron has a quadrupole anisotropic intensity distribution that we are able to measure a net polarized signal from the CMB and during reionization the number of free electrons increase. The information of the polarization makes it possible to estimate the evolution of the optical depth $\tau(z)$, from the epoch of decoupling to the present universe. It is beyond the scope of this master-thesis to go into the complicated details of how to measure the polarized intensity of the CMB. I will just briefly tell here, what it says about the ionization history of the universe. According to Page et al. (2007) and previous results, reionization occurred at redshifts between $11 < z_r < 30$ (95% CL). A model of the ionization history can be seen in figure 1.3, which shows the ionization fraction and the optical depth as functions of redshift. That reionization started as early as $z \sim 30$ seems to be evidence for that it was the first massive stars which started the reionization of the Universe.

1.4 The Formation of The First Stars

Since we believe that it was the first stars that started the reionization of the Universe, it seems appropriate to give short description of how they possibly have formed.

The oldest stars in our present-day universe are located in the globular clusters and in the halos in the outskirts of galaxies like the Milky way. These are what we call Population II stars, with a low metallisity contend compared to the more metal rich Population I stars like our sun. However, the Population II stars cannot have been the very first stars to have formed after the Big Bang. As described above the elements that came out of the BBN was only hydrogen, helium and tiny amounts of lithium and beryllium. Hence, those first stars must have contained only these four elements. Our knowledge of the present-day star formation in the Galaxy tells us that metals plays an important role of cooling the molecular clouds which is necessary for the clouds to become dens enough for stars to start forming. No cooling means no star formation, because cooling is a necessary mechanism to form molecular clouds where the gravitational instability can occur. So *how* did the first stars, also called the zeroth-generation stars, form? We have to come up with some idea, how to make cooling occur in a gas of only hydrogen, helium and the smattering of other light elements produced in the Big Bang. We need cooling for the gas to become dense enough so that stars can form. To day we believe that the solution is that there were a small, but nonzero, population of free protons and electrons remaining after recombination had occurred, *i.e.* for $z < z_{rec}$. Such free protons could then combine

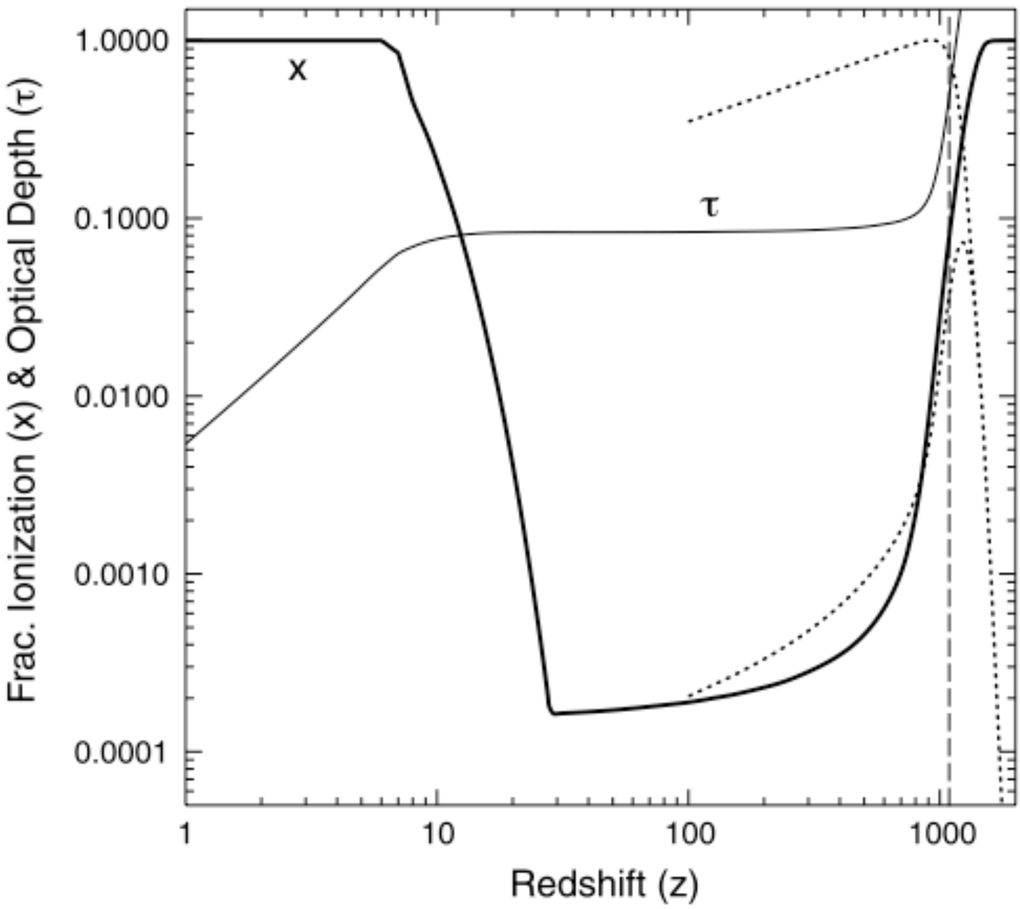

Figure 1.3: Model of the ionization history of the universe. The line marked with an "x" is the ionization fraction $x = n_e/n$, where n_e is the number of electrons and n the number of protons. The line marked τ is the net optical depth $\tau(z)$. The vertical dashed line marks the redshift of decoupling $z_{dec} = 1088$. The two dotted curves are respectively the term $(\exp(-0.3\tau(z)) - \exp(-\tau(z)))\sqrt{1+z}$ (top curve) and the term $(6\exp(-\tau(z)) + \exp(-0.3\tau(z)))\sqrt{1+z}$ (bottom curve). These two term will, when integrated over all z, $[0, \infty]$ give the ratio between the polarization anisotropy and the temperature signal in flat cosmology. From this model we see that the reionization occurred at redshifts between $11 < z_r < 30$ (95% CL) (Page et al., 2007). The figure is take from Page et al. (2007).

with the neutral hydrogen to form H_2^+ which again can combine another hydrogen atom to form H_2. This would lead to a small fractional H_2 abundance (Stahler and Palla, 2004) of order 10^{-7}. Later on, when the energy of the CMB had drop, the free electrons would increase the H_2 abundance an order of magnitude through the formation of H^-, which again can combine with neutral hydrogen to form H_2. Remember that when this is happening the gas is settling onto the already formed dark matter structure. At some point, we believe, that the fractional abundance in H_2 reaches about 10^{-3}, when the gas density n_H is of the order 10 cm^{-3}, in the collapsing structure. This is a critical point where emission in the rovibrational lines then creates a sharp drop in the temperature, which stabilizes near 200 K (Stahler and Palla, 2004). This event may have occurred at redshifts as early as $20 < z < 30$.

1.5 Reionization and The End of The Dark Ages

The question of what kind of objects or what kind of mechanisms are responsible for keeping the IGM ionized is the key subject of this thesis. I will discuss these things in this and the following sections.

As mentioned earlier, the Universe entered a period called the dark ages, after decoupling at a redshift of $z_{dec} \sim 1100$. However, because of Compton scattering, matter and radiation were still able to interact and exchange energy until a redshift of $z \sim 375$. After this redshift radiation and matter cooled separately until the first stars started to form at a redshift of $z \sim 30$. No sources of optical emission were present in the Universe in this dark ages epoch, but the neutral hydrogen did radiate 21-cm emission which can give us a chance to get information about the hydrogen distribution during the dark ages and the period of reionization. Simulations of the expected distribution of neutral hydrogen through the reionization epoch have been carried out by Furlanetto and collaborators (Furlanetto et al., 2004). Their are also projects underway which aim at observing redshifted 21-cm line. In 2009 the last of the LOFAR project radio telescopes were completed in the Netherlands. The LOFAR projects is an international project with a number of radio telescopes being build in different European countries. These telescopes can work together as a interferometric array of radio telescopes. LOFAR works at radio frequencies from $\sim$ 10-240 MHz which will give us the opportunity to search for the redshifted 21-cm line from the reionization epoch, in the redshift range $z \approx 5.8 - 140$.

As mentioned in the previous section, the first stars were probably very massive and short lived and radiated UV emission into the surrounding neutral hydrogen gas. These stars died in violent supernovae, sending out X-ray emission from the remnant and the compact object formed in the collapse. Massive black holes started to form in the centers of proto-galaxies and accreted the surrounding gas. This process caused these active galactic nucleus (AGN) to radiate very energetic ionizing photons into the IGM. All these processes created bobbles of ionized gas an as times went on, the bobbles expanded and started to overlap. This is how most astronomers believe that the dark ages ended and the IGM started to become ionized. Back in 1965

James Gunn and Bruce Peterson described a way to observationally determine how much of the diffuse intergalactic hydrogen was still neutral along the line-of-sight by examine the spectra of a certain type of AGN called quasar (QSO) (Gunn and Peterson, 1965). Before I explain how test works I will give a short description of the Lyman-α absorption systems that often can be seen in QSO spectra.

1.5.1 Lyman-α Absorption Clouds

Quasars are among the most luminous objects in the Universe and they have a non-thermal continuum spectra that extend into the far UV and X-ray wavebands. The observed spectra of a QSO is shown in figure 1.4. The upper part of the figure illustrate how the distant light from the QSO travel through the IGM which leave its mark on the spectrum of the QSO. Different "things" in the IGM leave different imprint on the QSO spectra. In the lower part of figure 1.4 which shows the spectrum, we can see the Lyman-α (Lyα) emission line from the QSO it self, at an observed wavelength of $\sim$ 4850 Å, since we know the rest wavelength of the Lyα line to be 1216 Å, we can find the QSO redshift to be, $z = (4850\ \text{Å}/1216\ \text{Å}) - 1 = 2$. Now, on the short wavelength side of the Lyα line, we see numerous absorption lines. These lines are called the Lyα forest and is imprinted on the spectrum by Lyα absorption clouds along the line-of-sight towards the QSO. That is because the photo-excitation cross-section of the Lyα transition in the hydrogen atom is large. When a photon with a wavelength $\lambda <$ 1216 Å leaves the QSO and travel through space, it will be redshifted due to expansion of the Universe. At some point in space, its wavelengths will be shifted to 1216 Å and if their, at this particular point in space, is a Lyα absorption cloud with neutral hydrogen column density in the range $N_{\rm HI} \sim 10^{12} - 10^{17}$ cm^{-2}, then the photon will be absorbed with high probability. Since Lyα clouds with this kind of density range are very common (as trees in a forest) they are able to create all these narrow absorption lines we see in spectra in figure. The closer the absorption line in spectra is to the Lyα emission line, the closer the cloud, responsible for making the line is to the QSO. So the absorption lines to the leftmost part of the spectrum are those which are created by clouds closest to us, because photons from that part of the rest-frame spectrum had to travel the longest to be shifted to the wavelength of the Lyα transition. QSOs at redshifts $z \sim 1$ show almost no absorption lines because the IGM is close to being fully ionized.

At a observed wavelength of $\sim$ 4150 Å in figure 1.4, we can a much broader absorption line with damped wings. This is the imprint of a damped Lyman-α system (DLA) which are rare. The neutral hydrogen column density of DLAs are $N_{\rm HI} \geq 2\times10^{20}$ cm^{-2}. These systems are associated with galactic discs and sometimes they show Lyα emission at the absorption line center of the QSO, which indicate star formation in the DLA. Lyα absorption clouds with intermediate column densities of $N_{\rm HI} \sim 10^{17} - 10^{20}$ cm^{-2}, which is between the Lyα forest and DLAs, are called Lyman-limit systems (LLS). When a LLS is present in a QSO spectrum it can be seen as a break in the continuum. In the observed QSO spectrum, the break will be at the redshifted 912-Å Lyman limit.

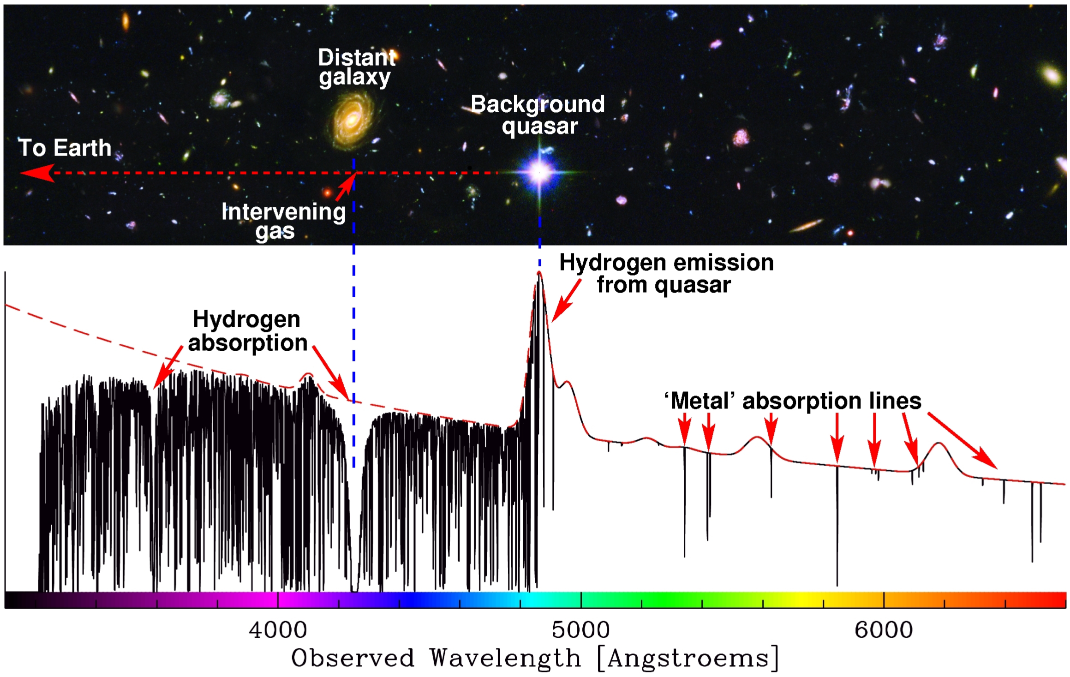

Figure 1.4: The upper part of the figure illustrate how the light from a distant QSO travel through the IGM. The IGM leaves an imprint on the spectrum of QSO, which is show i the part of the figure. See the text for an explanation of the absorption lines. The figure is taken from the ESO home page (http://www.eso.org/j̃liske/qsoal/)

The number density of Lyα absorbers increase with cosmic epoch and can be characterised by a power-law distribution as a function of number vs. redshift. The Lyα forest systems increase faster with increasing redshift than the LLSs do. However, when we observe quasars which light are reaching us from as distant redshifts as $z \sim 6$ we are starting to see the effect of reionization of the IGM in the spectra of the QSOs.

1.5.2 The Gunn-Peterson Test

If the line-of-sight to a QSO pass through a diffuse IGM, which has sufficiently large column densities of neutral hydrogen, the continuum on the blue side of the QSO Lyα emission line will be depressed due to the very high Lyα absorption. So if we imagine a QSO so distance, that its light is reach os from the end of the epoch of reionization, we would expect the imprint of the partially neural medium to be that all continuum emission on the blue side of the Lyα line is being absorbed. This is what James Gunn and Bruce Peterson predicted back in 1965 and astronomers have since tried to detect this trough in the UV continuum of high redshift QSOs. Finally, in 2001 Becker et al. (2001) report that they do detect the Gunn-Peterson trough in a QSO spectrum at $z = 6.28$, which they compare to 3 other QSO spectra at $z \sim 6$. Figure 1.5 show these 4 QSO spectra. QSOs are not standard candles, so before we can compare spectra of different QSOs, we need to normalize them. Another thing is, as I mentioned earlier the number density of the Lyα forest increase with redshift. This means that we would expect the UV continuum of high z QSOs, to be largely absorbed by discrete Lyα clouds. Becker et al. (2001) take these things into account and still find zero continuum flux in the bottom QSO spectrum in figure 1.5. They interpret this result as the detection of a Gunn-Peterson trough and conclude that the Universe is approaching the reionization epoch at $z \sim 6$. However, this detection has been disputed by others (Songaila, 2004) and is still being debated.

1.5.3 The Proximity Effect

We can also use QSO spectra to estimate the intensity of the diffuse ionizing background. It has been found that there is a deficit of Lyα absorbers with redshift close to the Lyα emission line of the QSO when we analyse the Lyα forest in the spectrum in a statistical manner. The reason for this phenomenon is that the Lyα forest clouds that are close to the QSO, has a higher degree of ionization due to the proximity of the QSO, than the clouds that are farther away. If we know the luminosity of the QSO, we can estimate how much of the ionization is due to the QSO and how much is caused by the intergalactic UV background (UVB). Thus, the proximity effect enables estimates of the UVB. Bajtlik et al. (1988) found that the UVB intensity is $\sim 10^{-24}$ erg s^{-1} cm^{-2} Hz^{-1} sr^{-1} at the Lyman limit for $z \sim 2-3$, which correspond to a photoionization rate of $\Gamma_{\rm HI} \sim 0.3 \times 10^{-12} - 2 \times 10^{-12}$ s^{-1}. Bajtlik et al. (1988) could account for this value of the photoionization rate $\Gamma_{\rm HI}$, by the amount of ionizing radiation coming from QSO population at $z \sim 2-3$. However,

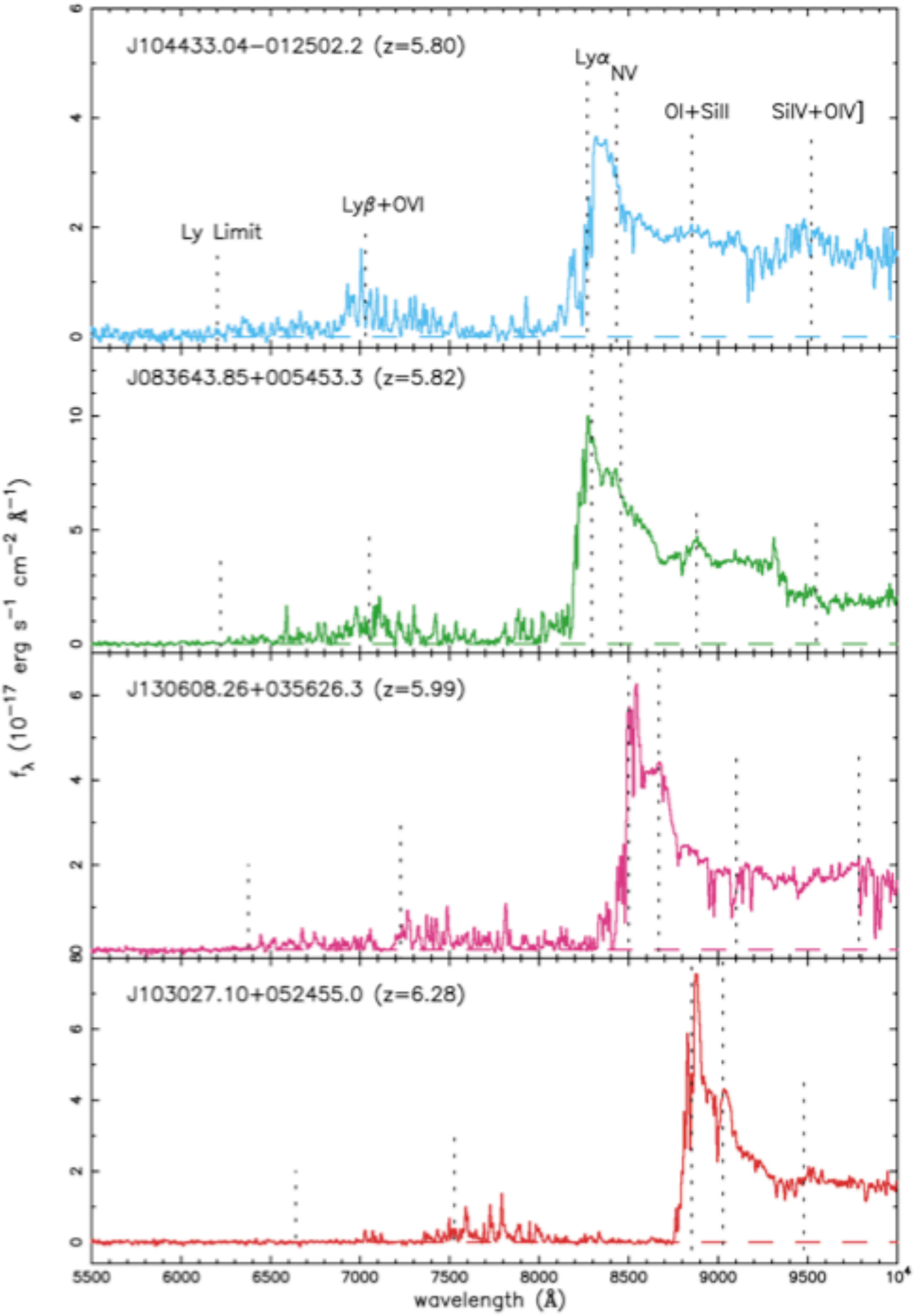

Figure 1.5: The figure show 4 spectra of 4 quasars with increasing redshift from the top and down. All 4 QSOs have very high redshift ($z \sim 6$). The 4 spectra are normalized to the observed z-band flux. We can see that the continuum on the blue side of the Lyα emission line is depressed with increasing redshift until it is gone at the bottom spectra at $z = 6.28$. This is seen as evidence for the detection of a Gunn-Peterson trough. The figure is taken from Becker et al. (2001).

the population of luminous QSOs seems to decline abruptly beyond redshift $z \sim 3$ and unless Γ_{HI} decline by the same factor, something else must contribute to Γ_{HI}. A more recent value of the photoionization rate, estimated from the a large sample of QSOs is reported by Dall'Aglio et al. (2009). They find a value of $\Gamma_{\mathrm{HI}} = 10^{-10.78}$ s^{-1} which is constant in the redshift range $z = 2 - 4$. Dall'Aglio et al. (2009) argue that this higher value which is constant out to $z = 4$ can be accounted for by arguing that star forming galaxies are contributing to the intergalactic UVB. However, all these numbers are still vividly debated among astronomers and it is still not clear today what the sources of the ionizing background are at redshifts $z > 3$. One of the most likely sources are star forming galaxies and proto-galaxies. However, it has also been proposed that decaying dark matter particles could deliver ionizing photons to the ionizing background, see below.

1.6 Decaying Dark Matter Particles

During the 1990th, the English scientist Dennis Sciama and collaborators suggested that decaying neutrinos could be responsible for creating the ionizing photons needed to photo-ionize the IGM, see *e.g.* Sciama (1998). This decaying neutrino theory is based on three parameters, the rest mass m_ν of the decaying neutrino, its radiative lifetime τ, and the monochromatic energy E_γ of the decay photon in the rest-frame of its parent neutrino. In the paper Sciama (1998), it is also assumed that $E_\gamma = 0.5 m_\nu$. In the same paper, Sciama derives an upper limit on τ using the local mass density of neutrinos and find the value $\tau \leq 2 \times 10^{23}$ sec. He finds the same value for the lower bound from the extragalactic background at 1500 Å and conclude that $2 \pm 1 \times 10^{23}$ sec. From upper limits on the extragalactic hydrogen-ionizing background at various redshifts, he find the monochromatic energy of the decay photon to be $E_\gamma = 13.7 \pm 0.1$ eV which is crucial, since such photons are energetic enough to ionize the hydrogen in the diffuse IGM. The theory predict that the emission from the decaying neutrinos should be present outside the earth atmosphere and the Spanish EURD detector onboard the MINISAT 01 spacecraft, measured the diffuse UVB in the relevant bandpass of $890 - 915$ Å. In 2001 Bowyer et al. (2001) reported that the analysis of the EURD data, had shown that no such emission was found. They concluded that the EURD data appear to be completely incompatible with the Sciama model of radiative decaying massive neutrinos.

1.7 Finding High Redshift Galaxies

Since it do not seem to be likely, that decaying dark matter particles can be responsible for the reionization rate, seen at high redshift, we are left with star forming galaxies. In this section, I will discuss how we can detect high redshift star forming galaxies.

When we take deep images of our Universe they will in general contain a variety of objects, like foreground stars in our own galaxy, nearby galaxies in our cosmological backyard and maybe some distant young galaxies, whose light have traveled for billions of years to reach us from the young universe. It then becomes very important for us to distinguish between the different kinds of objects in the image, if we want to interpret what we observe. Stars can *e.g.* often be identified by a point-like profile compared to galaxies which has a more flat or extended profile. So the biggest problem is usually to distinguish between galaxies of different redshifts. There are several methods of finding high redshift galaxies and each method will explore different classes of galaxies.

1.7.1 The Lyman Break Technique

This method is probably the most common and successful in finding star forming high redshift galaxies, and it has been used for more than a decade (Steidel et al., 1996). The light from star forming galaxies are intrinsically dominated by the young massive stars formed and they send out most of their energy as light in the blue and UV part of the spectrum. Since the young galaxies also contain large amounts of neutral hydrogen, HI, the majority of the photons with wavelength less than 912 Å, will be absorbed before leaving the galaxy. This means that the galaxy spectrum will have a clear break at 912 Å in their rest frame. Because the light from these galaxies are redshifted we can observe this "Lyman Break" from earth based telescopes using broad-band filters, where we exploit that the galaxies will not show up in a filter that probe the light below 912 Å in the rest frame but will have a visible continuum at the long wavelength side of the break. The Lyman Break Technique is illustrated in figure 1.6.

1.8 Lyman-α emission as a Probe for Early Star Formation

Another way of finding star forming galaxies, is to look for objects with strong Lyα emission. Generally speaking we know three different kinds of situations that leads to Lyα emission. We have seen Lyα emission from quasars and AGNs, from which we observe a strong UV continuum that ionize the hydrogen and hence, leads to Lyα emission. In the last decade or so, it has been suggested that "cold accretion" can be responsible for creating Lyα emission. The theory of cold accretion propose that hydrogen falling onto a dark matter halo will be heated enough to be ionized. When it recombine Lyα emission will follow as a result of that. The first case of observation of extended Lyα emission, which best can be explained by cold accretion, was published by Nilsson et al. (2006). In this Letter the authors argue that AGN and "super-winds" resulting from supernovae can be ruled out, due to the fact that no continuum emission is present.

The most common source of Lyα emission is however star formation. Massive O and B stars sends out the majority of their energy in the blue and UV part of the spectrum. Since these stars have short lifetimes ($10^5 - 10^7$ yr), they are only found

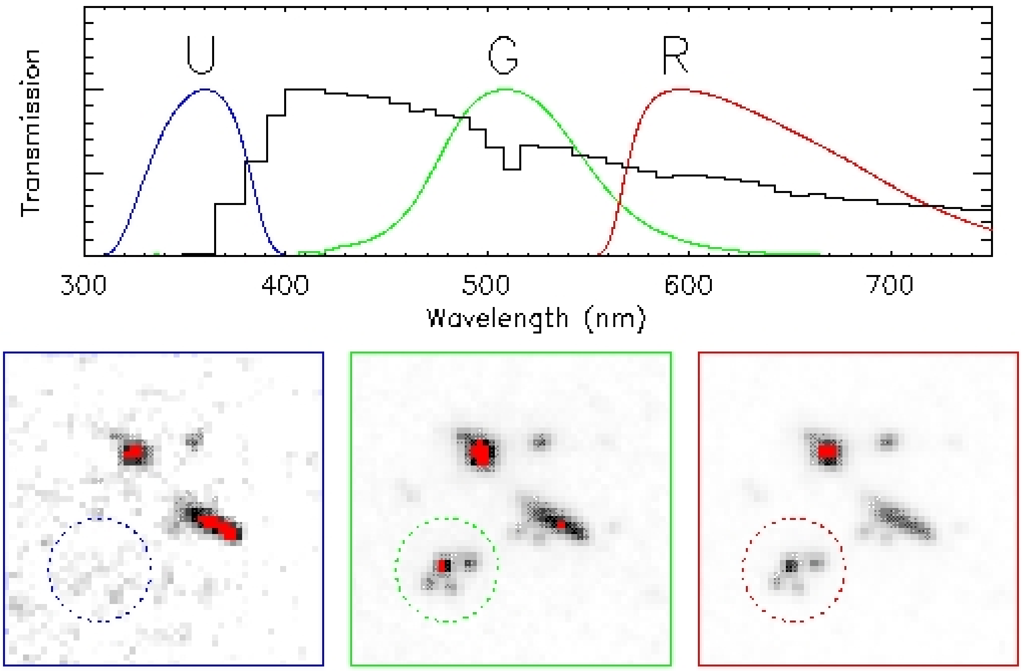

Figure 1.6: Illustration of the Lyman Break technic. The upper panel shows the typical shape of a galaxy spectrum. The Lyman Break which in the rest frame is located at 912 Å = 91.2 nm is here redshifted to $\sim$ 400 nm . On top of the spectrum three transmission curves for the broad-band filters U,G and R are shown, to illustrate the wavelength sensitivity range of the filters. The lower panel shows a LBG observed through these three filters. The galaxy marked with a dotted circle can clearly be seen in the G- and R-band, but does not showup in the U-band as this filter probes below the Lyman limit. Image credit: Johan P. U. Fynbo.

in star forming regions/galaxies. The Lyα emission comes partly from the stellar atmosphere, but also from the interstellar hydrogen gas that these massive stars easily ionize. When I in this thesis refer to Lyα emitters (LAEs), I will in general mean, young star forming galaxies. In this thesis I will investigate 18 such LAEs, to see if it is possible to measure any Lyman-continuum (LyC) emission coming from these young star forming galaxies. Before going into details about how to measure LyC emission and what other people have found, I will give a short description of how LAEs are detected using the narrow-band technique.

1.8.1 Finding LAE using the narrow-band technique

A narrow-band filter is a filter that allows only a small range of wavelengths to pass through and blocks out all other wavelengths. Since we are amine at detecting Lyα emission line objects, we choose what redshift we are probing, when we choose the narrow-band filter. One of the most common existing narrow-band filters is the OIII-filter with a central wavelength at 5105 Å. Using this filter, we are probing LAEs at a redshift: $z = (5105\ \text{Å}/1216\ \text{Å}) - 1 \approx 3.2$. Quality narrow-band filters with a high transmission are expensive, so astronomers have often used existing narrow-band filters at the telescopes they are using, like the OIII-filter. In order for us to find the LAEs we also need to observe the same field with broad-band filters, usually two. The broad-band filters are probing the continuum of the LAEs and we can hope to detect them by comparing the continuum flux with the LAE emission-line flux. Objects with a high flux ratio in the narrow-band compared to the broad-band are selected as LAE candidates. However, follow-up spectroscopy is needed before we can confirm a candidate. Because, nearby galaxies with other emission-lines can be detected as a candidate, if wavelength of this emission-line coincide with the narrow-band filter in the observed frame of the galaxy.

1.9 Measuring Lyman-Continuum Emission from High Redshift Galaxies

One of the challenges trying to observe Lyman-continuum (LyC) emission from high redshift galaxies, is that a large fraction of the LyC that succeed in escaping the galaxies, is being redshifted and absorbed in Lyα in the neutral part of the intergalactic medium (IGM) before it reaches us. That part of the emission is not contributing to the ionization of the IGM and we cannot observe it, because it is absorbed. It is believed that the Lyα absorption is caused by numerous discrete absorbing systems, as mentioned above. These absorbers are probably outer halos of galaxies, halo gas and a diffuse medium in the intergalactic space. These different components gives the IGM a clumpy nature, which mean that the intergalactic absorption fluctuates among the lines of sight. The consequence of this is, that it is impossible to predict the absorption for any given line of sight. However, we can use a statistical approach. What we can predict is, the average absorption and the standard deviation for many lines of sight. Inoue and Iwata (2006) use this statistical approach in a Monte Carlo simulations. Their results for the transmission of the LyC can be seen in figure 1.7. The figure shows the transmission averaged over the wavelength range $[880, 910]$ Å of LyC in the source rest-frame as a function of the source redshift. Both LyC absorption and Lyman series absorption is included in the simulation. The filled circles and the error-bars are the median and the central 68% of the distribution of the wavelength-averaged transmission of 10 000 lines of sight for each source redshift. The authors argue that the large dispersion is a consequence of the stochastic (random and independent) nature of the LyC absorption. The red cross in figure 1.7 is the LyC transmission measured by Steidel et al. (2001), based on the composite spectrum of 15 QSOs, see section 1.9.1.

Their has been different approaches in the astronomical community when it comes to measuring LyC emission from high redshift galaxies. The earliest attempts have been focused on using spectroscopy, *e.g.* Steidel et al. (2001) or Giallongo et al. (2002). Spectroscopy has the advantage of being able to measure the LyC level very close to the redshifted Lyman-limit where the redshifted LyC photons has a larger change of reaching us. This is because the average IGM opacity at the Lyman-limit is not as large as it is at shorter wavelength because of the Lyman-valley (Møller and Jakobsen, 1990). Fernández-Soto et al. (2003) use the U_{300}, deep broad-band images of the Hubble Deep Field North, but experience problems with their U_{300} flux being contaminated with non-ionizing UV photons. Therefore, narrow-band imaging appears to be a suitable compromise between the lower opacity offered by spectroscopy and the depth of detection offered by broad-band imaging as shown by Inoue et al. (2005).

1.9.1 Previous Results

One of the first successful attempts on direct detection of LyC emission from high redshift galaxies was done by Steidel et al. (2001). They report the finding of significant LyC flux in the composite spectrum of 29 LBG. These 29 spectra with an average redshift of $\langle z \rangle = 3.40$ were chosen among 875 spectra of LBG obtained with Keck telescopes. The 29 LBG were pict out using the criteria that they all have $z \geq 3.300$ and $R \leq 25.0$ (AB magnitude). They also discarded spectra obtained under poor conditions or with contamination form neighboring objects. Using these criteria Steidel et al. (2001) end up with a composite spectrum of 29 LBG chosen from the bluest quartile of the observed LBG UV colors. In order to estimate the escape fraction of LyC (f_{esc}) they need an estimate of how much of the measured LyC emission is absorbed along the lines-of-sights by intervening material not directly associated with the galaxies. They do this using of sample of QSOs. Remember that QSOs have a non-thermal spectrum which a continuum that extend all the way through UV and into x-ray emission. The composite QSO spectrum is effectively an average over 15 lines of sight for QSOs with a mean redshift $\langle z_{QSO} \rangle = 3.47 \pm 0.14$. To estimate the change in net opacity due to intergalactic material between 1100 Å and 900 Å in the rest frame, they adopt the intrinsic QSO SED shortward of 1050 Å

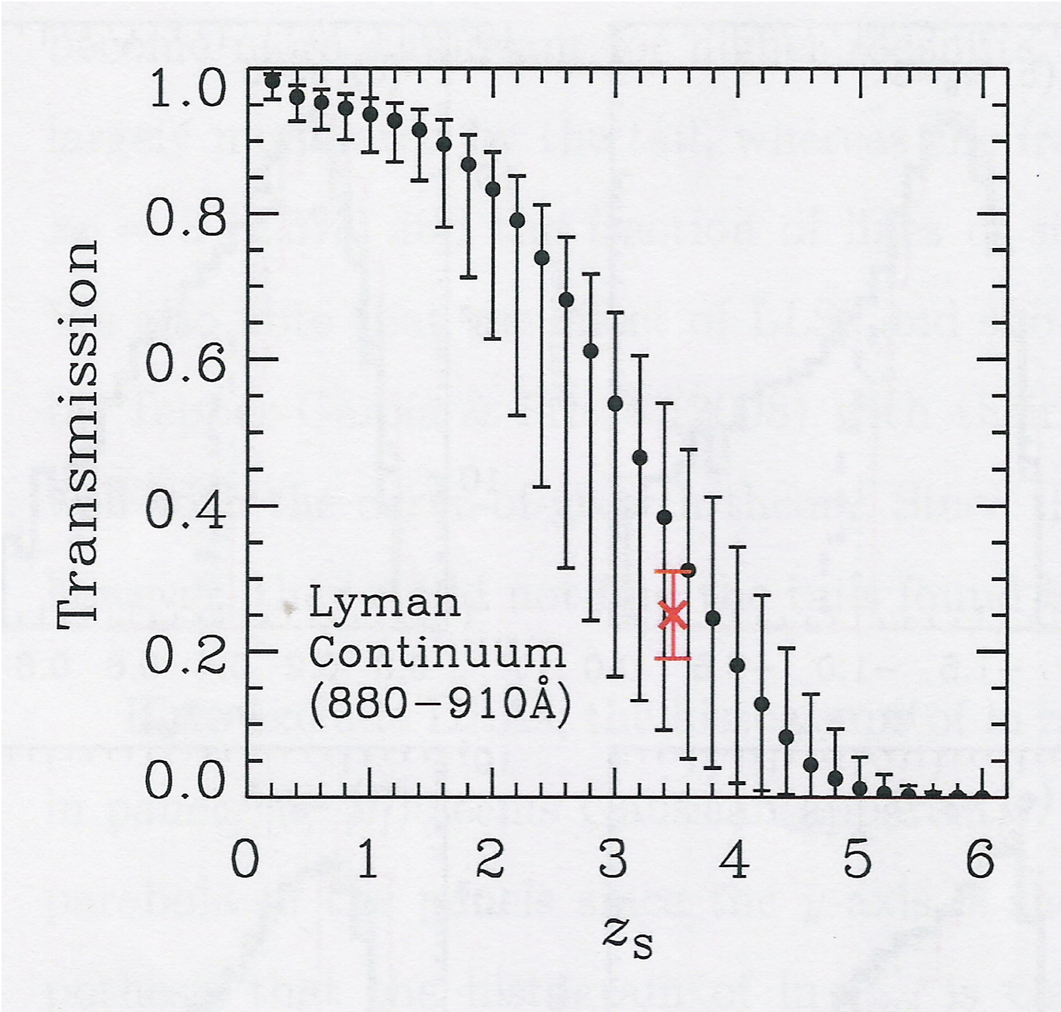

Figure 1.7: Transmissions of the LyC from the Monte Carlo simulation in Inoue and Iwata (2006). The transmission is averaged over the LyC [880, 910] Å in the source rest-frame. The horizontal axis is the source redshift. The filled circles and vertical error-bars are median and the central 68% range of the wavelength-averaged transmissions for 10 000 lines of sight generated in the Monte Carlo simulation. The red cross shown, is the estimation by Inoue and Iwata (2006), based on the composite spectrum of 15 QSOs at $\langle z \rangle = 3.47$ by Steidel et al. (2001). Figure taken from Inoue and Iwata (2006).

suggested by Madau et al. (1999), which is a power-law, $f_\nu \propto \nu^{-1.8}$. They observe a change in the in the QSO continuum level by a factor of 3.7 ± 0.2, between the [1060, 1070] Å interval and the [880, 910] Å interval. The intrinsic component of the flux decrement is estimated from the power-law, to be a factor of 1.5. This means that the inferred flux decrement at 900 Å relative to that at 1100 Å is an factor of 2.5, due to the intervening material along the line of sight. They use this factor to correct the observed intrinsic flux density ratio $f[1100]/f[900] = 9.4 \pm 2.0$, obtained from the composite LBG spectrum. Here they take the Lyα line blanketing in the [1060, 1170] Å interval into account. Steidel et al. (2001) define the escape fraction (f_{esc}), as the fraction of emitted 900 Å photons that escape the galaxy without being absorbed by interstellar material divided by the fraction of 1500 Å photons that escapes. So after they correct for the small difference in unabsorbed flux between 1500 and 1100 Å, they find that the intrinsic flux density ratio for LBG is $f[1500]/f[900] = 4.6 \pm 1.0$, which they find to be unexpectedly large and make the assumption that a better factor is 3. They find the observed flux density ratio to be $f[1500]/f[900] = 17.7$. This implies that the fraction of UV ionizing photons that are escaping the galaxy is more than 50% relative to the non-ionizing UV photons that escapes. We can do the calculation:

$$f_{\mathrm{esc,rel}} = \left(\frac{3}{17.7}\right)\exp(1.5) = 0.76$$

The authors state that this is unexpectedly large and may possibly be due to the fact that the 29 LBG spectra, that were chosen are from the bluest quartile of the observed LBG population, implying that these galaxies are younger and/or less dusty. Since this would increase the likelihood of getting LyC photons out into the intergalactic medium.

The first attempt on detecting LyC emission from high redshift star forming galaxies using narrow-band photometry was preformed by Inoue et al. (2005). Using the OII+44 narrow-band filter at the FORS instrument on ESOs Very Large Telescope (VLT) (the same filter that is used for the observations described in this thesis), the authors are observing to galaxies, HDFS 1825 and HDFS 85 in the Hubble Deep Field South. Preforming spectroscopic observations with FORS2 in MXU mode, they measure the redshift of the to galaxies to be $z_{\mathrm{HDFS\ 1825}} = 3.275$ and $z_{\mathrm{HDFS\ 85}} = 3.170$. Inoue et al. (2005) are also using data from VLT/ISAAC and HST/WFPC2 which gives them observations of the two galaxies in the broad-band filters: U_{300}, B_{450}, V_{606} and I_{814}. The authors does not find any significant LyC flux from the two galaxies, but they can put an upper boundary on the LyC emission. They estimate the intrinsic non-ionizing to LyC luminosity density ratio $(L_{1500}/L_{900})_{\mathrm{int}}$, to be a factor of 3.0. This number seems to agree with *Starburst 99* models, where they assume a constant star formation rate and a Salpeter initial mass function (IMF) in the mass range of $0.1 - 100$ M$_\odot$, and variate the metallicity in the range $0.001 - 0.02$, the upper boundary being the solar value. They also vary the galaxy age and find that these models gives them intrinsic luminosity density ratios in the range $(L_{1500}/L_{900})_{\mathrm{int}} = 1.5 - 5.5$. The value of 3.0 adopted, is in this range and in agreement with Steidel et al. (2001). Before they can put an upper boundary on the escape fraction f_{esc}, they need to estimate the IGM opacity for the LyC. Using a model based on the number distribution function of Lyα forest and the denser HI clouds they find $\tau_{\rm IGM} = 1.32$ and $\tau_{\rm IGM} = 1.99$ for HDFS 85 and HDFS 1825 respectively. They find the upper bounds for the relative escape fractions of the two galaxies to be < 0.72 and < 2.16 respectively and they find the upper bounds for $f_{\rm esc}$ to be < 0.17 and < 0.38.

The first successful detection of LyC from individual galaxies were reported by Shapley et al. (2006). In the SSA 22a field they investigate 14 bright LBGs with $23.0 \leq R < 24.5$ and redshift range $z = 2.756 - 3.292$. They detect LyC emission in the spectra of two LBGs in their sample and estimate the relative escape fraction $f_{\rm esc,rel}$ of these two LBGs to be respectively 0.43 and 0.72. However, the average $f_{\rm esc,rel}$ of the hole sample is only found to be 0.094.

A more resent detection of LyC emission and one that also detect LyC from LAEs is reported by Iwata et al. (2009). Using Subaru/Suprime-Cam narrow-band imaging they investigate a large sample of 198 star-forming galaxies at redshift $z \sim 3$ in the SSA22 proto-cluster region. They find LyC above 3σ within a $1''.2$ diameter aperture from 16 objects, 10 of which is LAEs and 6 LBGs. Iwata et al. (2009) also measure a 2.95σ flux-level from another LBG, which is detected by Shapley et al. (2006) and include that in their sample, which brings the total number of detected objects to 17. All 10 LAEs have a spectroscopically confirmed emission-line at ~ 4970 Å, which is where the Lyα line will be if the 10 LAEs are indeed LAEs at $z \sim 3.09$. However, the authors do not have spectroscopic data for a large enough wavelength range, for them to exclude the possibility of the LAEs being AGNs at a lower redshift. They only estimate the escape fraction $f_{\rm esc}$, of the 7 LBGs. They use two different values for the intrinsic UV to LyC flux density ratio; the value 3, which is the one used by Steidel et al. (2001) and Inoue et al. (2005), and the value 1.07, which they find from the bluest model galaxy SED generated with the Starburst 99 code. Using the values 3 and 1.07 the find relative median escape faction $f_{\rm esc,rel}$of their sample, to be 0.83 and 0.30 respectively. The numbers have been corrected for IGM attenuation using a median optical depth for the LyC of $\tau_{\rm IGM} = 0.59$. They finally estimate the $f_{\rm esc}$ to be 0.20 nd 0.07 respectively.

I have put in the numbers from these articles in table 1.1 for comparison.

Reference	Sample	Redshift	$\left(\frac{L[1500]}{L[900]}\right)_{\rm int}$	$\left(\frac{f[1500]}{f[900]}\right)_{\rm obs}$	$\tau_{\rm LyC}^{\rm IGM}$	$f_{\rm esc,rel}$
Steidel	29 LBGs	$\langle 3.40 \rangle$	3	17.7	1.5	0.76
et al. (2001)	Average					
Inoue	2 LBGs	3.275	3	> 10.17	1.99	< 2.16
et al. (2005)	Individual	3.170	3	> 15.57	1.32	< 0.72
Shapley	2 LBGs	3.067	3	7.5	0.59	0.72
et al. (2006)	Individual	3.151	3	12.7	0.60	0.43
	Average $\langle 14 \rangle$	$\langle 3.06 \rangle$	3	58	0.60	0.094
Iwata	7 LBGs	$3.04 < z < 3.31$	3	6.6 median	0.59	0.83
et al. (2009)	Individual		1.07	6.6 median	0.59	0.30

Table 1.1: This table list the examples of estimated $f_{\rm esc,rel}$ together with other relevant numbers from the literature described in this section.

Chapter 2

Observations

The data for this master thesis are based on observations carried out with the Very Large Telescope (VLT). The VLT is located at the top of Mount Paranal in Chile and operated by the European Organization for Astronomical Research in the Southern Hemisphere also known as European Southern Observatory (ESO). In this chapter, I will give a description of the VLT and the FORS instrument setup used.

2.1 The VLT

The VLT consist of four telescopes which can work independently or in a combined mode. Each telescope has a primary mirror diameter of 8.2 meter and in the combined mode collect light equivalent to one telescope with a primary mirror of 16 meters. All four telescopes are alt-azimuth mounted so it is possible to cover nearly the whole sky above the horizon. Each telescope is equipped with different instrument mounted at the various foci (Cassegrain, Nasmyth and Coudé).

The FORS1 instrument used for these observations was mounted at the Cassegrain focus of UT1. FORS is the visual and near UV FOcal Reducer and low dispersion Spectrograph and can be used in 6 different observing modes including direct imaging mode which has been used for obtaining this data. FORS1 works in the wavelength range 330-1100 nm.
During the spring of 2007 a new and improved mosaic of two CCDs was installed to replace the old single CCD and since I have used data from 2005 up to 2008 I will give a short description of both the old and new CCDs. For a general review of how a CCD works, see appendix A

2.1.1 CCD setup before 2007

The old FORS1 detector was a 2048×2048 Tektronix CCD, with a pixel size of 24×24 μm. Since the observations was carried out during service time, only the default setup was available. In direct imaging mode this means that the CCD was

Figure 2.1: The VLT at the top of Paranal, from left to right: Unit Antu, Unit Kueyen, Unit Melipal and Unit Yepun. Picture taken from ESO home page (http://www.eso.org/gallery/v/ESOPIA/Paranal).

read out from four different ports A, B, C, and D, located in the corners of the chip and with a high gain and a 1×1 binning. The gain, read out noise and conversion factors for each port is listed in the table 2.1 below.

2.1.2 New CCD setup

In February 2007 a new E2V CCD mosaic detector was installed for the FORS1 instrument and has been used for observations since April 7, 2007. The new double chip consist of two CCD's with 2048×4096 pixels with a pixel size of 15×15 μm and

Port	Gain	RON[e^-]	K[e^-/adu]
A	high	5.13 ± 0.11	1.37 ± 0.02
B	high	5.57 ± 0.11	1.70 ± 0.04
C	high	5.76 ± 0.10	1.62 ± 0.02
D	high	5.87 ± 0.15	1.73 ± 0.03

Table 2.1: Data for the old CCD

	Chip 1	Chip2
RON[e^-]	4.16	4.03
Gain	2.22 e^-/adu	2.37 e^-/adu

Table 2.2: Data for the new CCD

they are particularly sensitive in the blue range of the spectrum. The new FORS1 detector works in the wavelength range 3300-11000 Å. The observation was done in 2×2 binning readout mode using standard resolution which is $0.25''$/pixel. The field of view in this mode is $6.8' \times 6.8'$. The RON and gain for each chip is listed in table 2.2. The data in table 2.1 and 2.2 will be used in the chapter 3.

The data I have worked on, (reduced, stacked, calibrated and analyzed) were obtained in service mode from spring 2005 to spring 2008. All observations were done using the FORS1 instrument, mounted on unit Kueyen, in images mode with an OII-filter, here after NB_{LyC}. I have also used data from 2003 of the same field, published in Grove et al. (2009). This data was obtained in service mode using the FORS2 instrument, unit Yepun, also in image mode. I did not reduce or in any way calibrate this data, but used the images and the results published in Grove et al. (2009). These data give me observations of the field in the three filter bands OIII, V and R and is part of the "The Building the bridge Survey", Fynbo et al. (2003) and Grove et al. (2009). The aim of this survey is to establish a link between LBG, detected in emission and absorption systems, detected in the spectra of background QSOs, by observing the faint end of star forming galaxies at redshift, $z \approx 3$.

I will now give a brief summary of the results from Grove et al. (2009) and why and how this field was observed. I refer to section 1.8.1 for a more detailed review of how observation of LAE is carried out.

2.2 The field of BRI 1202-0725

The field of the bright quasar, BRI 1202-0725 ($z_{qso} = 4.70$), was chosen as part of the "The Building the bridge Survey", due to the presence of a Lyman-limit system along the line-of-sight towards the quasar. This Lyman limit absorber, which is found in the spectra of the quasar (Storrie-Lombardi et al., 1996), has the appropriate redshift $z = 3.2$, which is targeted by the survey. The astronomers involved in the survey chose this particular redshift because they could use an existing OIII-filter, which probes the Lyα emission-line at $z \sim 3.2$. The presence of this LLS indicate, that this is a good area of the sky to search for star forming galaxies, at this particular redshift.

Grove et al. (2009) uses the OIII narrow-band filter, here after $NB_{\mathrm{Ly}\alpha}$, to look for star forming galaxies with a Lyman-α emission line redshifted from the 1216 Å in the rest frame to 5107 Å in the observed frame, which corresponds to the central wavelength of this filter. The Bessel $V$and the special R filters are used as the on- and off-broad-band filters to measure the continuum emission. The measured filter

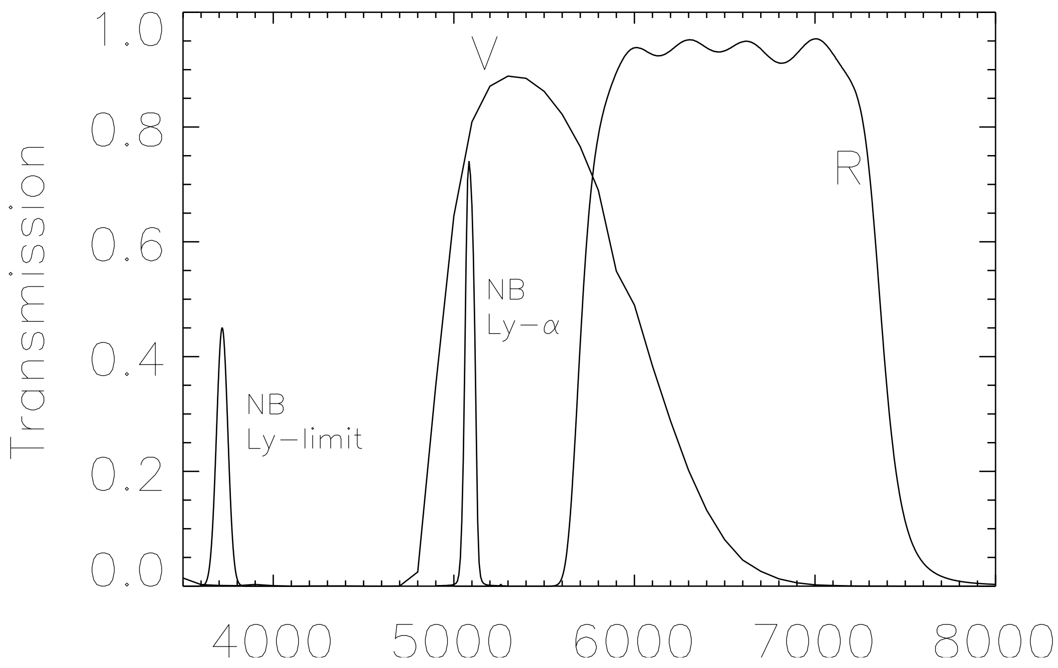

Figure 2.2: Transmission curves of the two narrow- and two broad-band filters used for the observations of the field of BRI1202-0725. The horizontal axis is the wavelength in Angstrom.

transmission curves for all four filters can be seen in figure 2.2. The NB_{LyC} filter was chosen so we will be able to measure Lyman-continuum emission from already detected LAE located at redshift $z \sim 3.2$. This narrow-band filter has a central wavelength of 3717 Å, which is just to the short wavelength side of the Lyman-limit in the rest frame of the LAEs at this redshift. Thereby measuring the emission reaching us, if any, from below the Lyman-limit at 912 Å in the rest frame redshifted to 3830 Å in the observed frame. There was no measured filter transmission curve for NB_{LyC} filter so I use a Gaussian function to model the filter curve which can be seen in figure 2.2. I have also summarized the filter characteristics for all four filters in table 2.3. In the table is also included the total exposure time for each filter. Grove et al. (2009) report that they find 3202 objects in the narrow-band (OIII) filter image, here after $NB_{\mathrm{Ly}\alpha}$. After comparison with model spectra of star forming galaxies shifted to the appropriate redshift, a sample of 25 LAE candidates were selected for follow-up spectroscopy. The multi-object spectroscopy (MOS) was carried out in visitor mode on March 21-23, 2004, with FORS2. Two grisms was used to get a wavelength coverage from 3600 Å to 7500 Å, see Grove et al. (2009) for details. The MOS were reduced and of the 25 LAE candidates, 18 were confirmed emission line objects. The field of BRI 1202-0725 and the 18 LAE are shown in figure 2.3. According to Grove

Filter name and ESO nr.	Centr./eff. wavelength	Peak trans.	FWHM	Total exp. time (hr)
NB_{LyC} (OII+44)	3717 Å	0.45	73 Å	28.4
$NB_{\mathrm{Ly}\alpha}$(OIII/6000+52)	5105 Å	0.74	61 Å	8.3
V(V_BESS+75)	5540 Å	-	1115 Å	2.9
R (R_SPECIAL+76)	6550 Å	-	1650 Å	1.6

Table 2.3: Filter characteristics of the four filter used in the observations. In all cases, the standard resolution collimator was used

et al. (2009) a candidate is confirmed if there is an emission line detected with at least 3σ significance at the correct position in the slitlet within the wavelength range corresponding to the filter transmission.

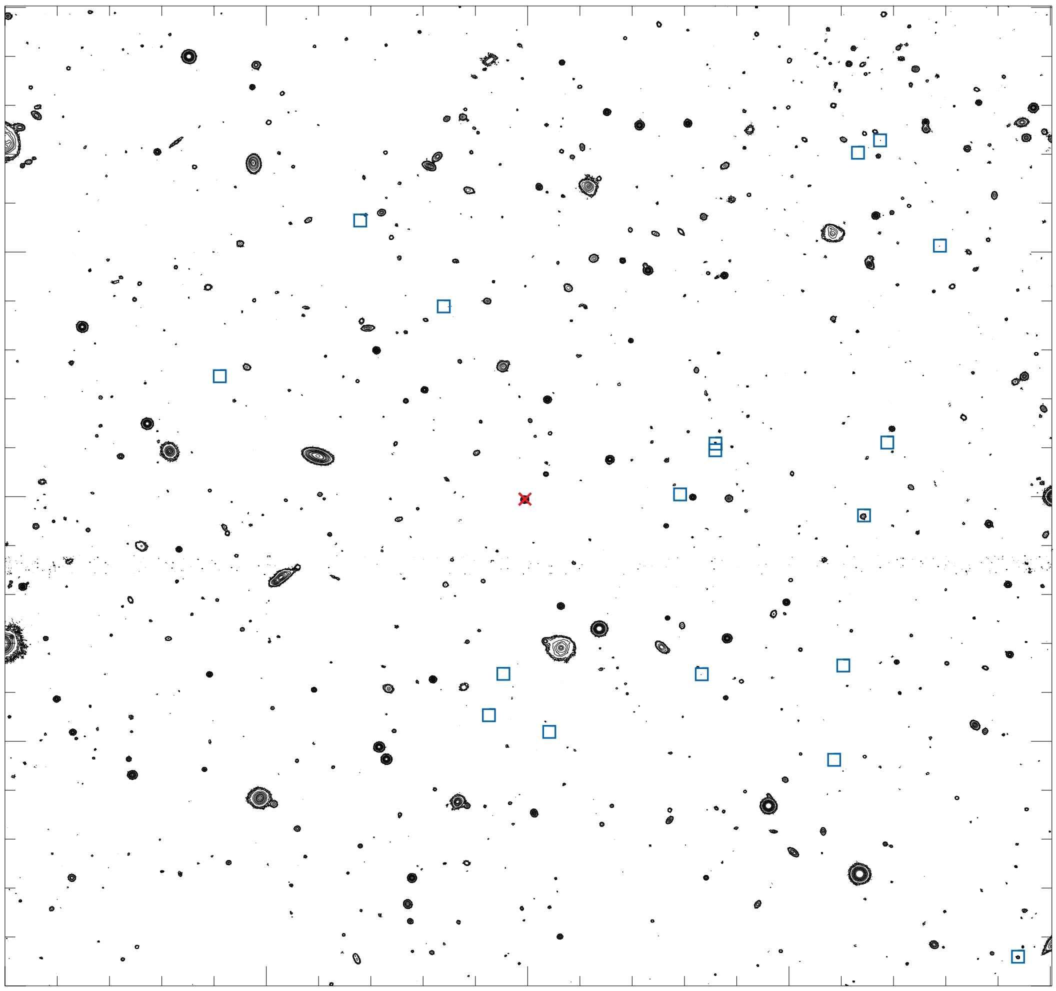

Figure 2.3: The 400×400 **arcsec**^{2} field surrounding the bright QSO, BRI 1202-0725, as observed in the $NB_{\mathrm{Ly}\alpha}$filter, from Grove et al. (2009). North is up and East is to the left. The QSO is marked by a "×" at the field center and the positions of the 18 spectroscopically confirmed LAE are shown with "□".

Chapter 3

Data Calibration

In this chapter I will give a description of the calibration and reduction methods of the bias, flat and science frames. I will also go through the process of combining the reduced science images into one. Finally, I will describe how I find the magnitude zero-point for the combined image using spectrophotometric standard stars.

3.1 Bias and Flat-Fielding

The data are obtained over several nights, stretching over a times span of 3 years, which included a change of the FORS1 CCD, thus complicated the calibration process a bit. In general there are five raw bias frames and four raw flat fields for each observing night, during the three years of observations, and consequently I made one master bias and one master flat for each observing night using the appropriate raw frames. However, for the year 2006, there are only five raw flats in all and they where taken on five different nights so I decided to combine all five flats from 2006 into one master flat and therefor I also combined all 13 raw bias-frames from 2006 into one master bias. This is not a serious problem, as the bias and flats are very stable, see the appendix B.1 and B.2 for a list of the master-bias and master-flats used in the reduction.

I have used a small IDL procedure to make the master bias. I read in the raw bias and subtract the mean of a stripe of the overscan area from each of the raw bias-frames. After this I calculate the master-bias by comparing the different bias-frames pixel to pixel and taking the median to use for the master frame so the master bias becomes the median frame of the raw bias' after subtraction of the overscan area.

In the same way as for the master-bias, I used a small IDL procedure to calculate the master-flats. After reading in the raw flats subtraction of the overscan area are done in the same way as for bias-frames, but of course also the bias is subtracted from each flat, using the master-bias calculated before. Then each flat is normalized by dividing it with the median of a section of the flat. In the end the master-flat is calculated as the median frame of the stack of normalized flats in the same way the master bias was calculated.

3.1.1 Calibration of Science Images

Finally I de-biased each science image using the appropriate master bias and corrected for pixel to pixel variations by dividing with the master flat.

3.2 Combining Science Frames

All the science images have now been reduced and we need to combine them into one stacked image. Again we will have to combine all the science images from the old chip into one separate image and data from new chips into another image and then combine these two images into one image. Prior to combining the data from the new double CCD, I assembled the data from each CCD into one image using the FORS1 standard software tool called *fsmosaic* which is part of the ESO FIMS tool packet.

The challenge of combining all the images is to find a optimal way to stack n images into one image. The process should be able to handle that the images in the stack in general will have slight offsets, different seeings, different sky background levels and also have different flux levels because of the varying airmass and observing conditions. The process should also be able to remove cosmic ray hits. The first step in this process is to subtracted the individual sky-level form each image in the stack. The sky-level in images n, is calculated as the median of a part of the image. After this, all the images is scaled so an object with constant flux will have the same flux in all n images and the measured coordinate offset is used to shift the n frames, to a common coordinate system. Now, with all images shifted, so that the same sky object is in principle located on (almost) the same pixels in each image. We then need a way to combine the n values of any given pixel into a final combined value. The combination should maximize the final signal-to-noise (SN) ratio for objects, for which the noise is dominated by the background shot-noise. *Why*? Because this is the best we can hope to do. We cannot get rid of the random and independent arrival of photons, but we can try to combine the images in such a way that we maximize the SN ratio for objects whose total noise is dominated by the background shot-noise. If we look at such an object in frame j we can express the variance as $\sigma_j^2 = sky_j + \mathrm{RON}^2$, where sky_j is the sky-level in frame j and RON is the readout noise, see appendix A. This is relevant because we want to give each science image a weight when we combine them. The optimal weight for frame j is given by the this variance times the square of the flux scale for that frame:

$$W_j = (sky_j + \mathrm{RON}^2) \times scale_j^2 \tag{3.1}$$

The flux scale is the normalizing factor that brings frame j into the same flux level (for a constant source) as the frame with the highest flux level. This scaling factor is found in same process that measure the pixel offset in both dimensions. I have illustrated the process of combining images in a flow diagram in figure 3.1. In general, when we look at a given pixel in frame j, it will have the value s_j and the hole set of n pixel will have the variance:

$$Var_j = scale_j^2 \times (s_j + sky_j + \mathrm{RON}^2) \tag{3.2}$$

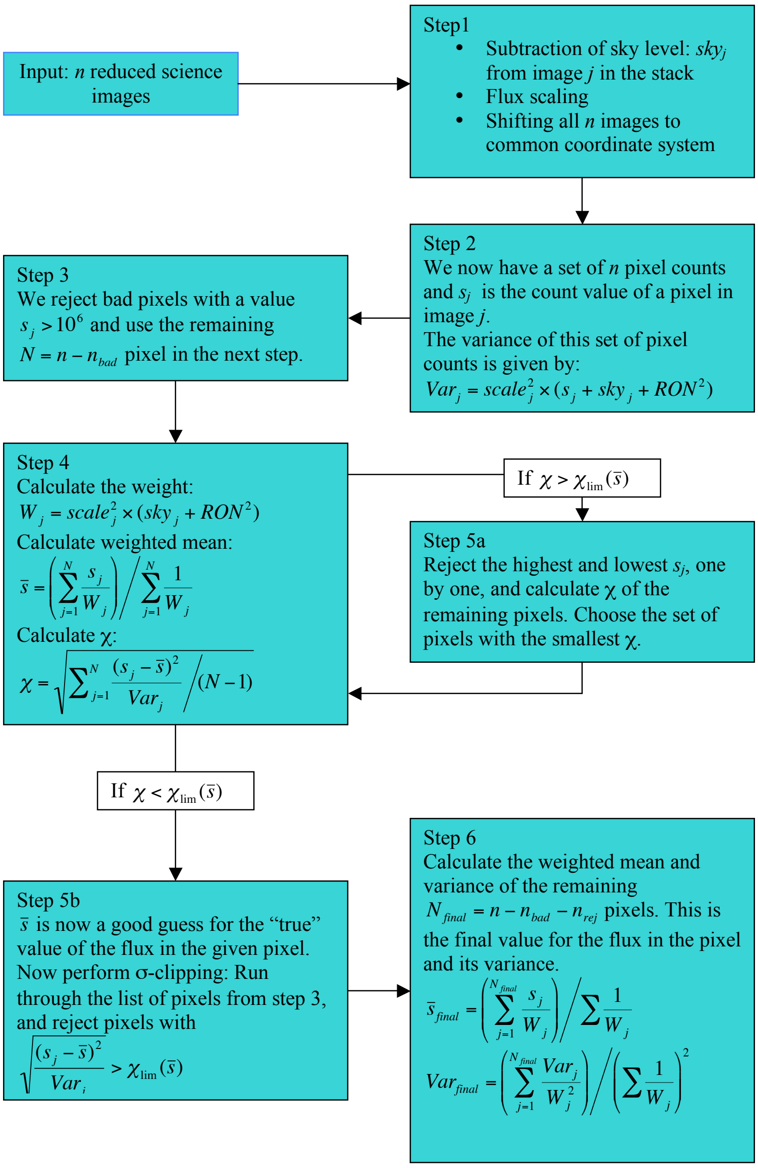

Figure 3.1: Block diagram describing the process used to combine the science images using σ-clipping.

We start by rejecting pixels in bad columns, hot pixel and other pixels for which we have a priori knowledge that they do not contain useful information. By inspection, we could see that a portion of where the two images from the new FORS1 double-CCD was put together, did not contain useful information. I chose to reject these areas by manually giving the relevant pixels a high ADU-value. The rejection-value chosen was 10^6 ADU. We then wish to calculate the optimally weighted average of the remaining $N = n - n_{\rm bad}$ pixels, using (3.1). We probably need to reject more pixels in the following, *e.g.* due to cosmics. On the other hand, we do not necessary want to reject all pixels that deviates much from the mean. *Why?* Because strong sources will naturally tend to have a large spread in pixel values from one frame to another. So the strategy we use is *σ-clipping* (Møller and Warren, 1993). The χ-function is given by:

$$\chi = \sqrt{\frac{\sum_{j=1}^{N} \frac{(s_j - \overline{s})^2}{Var_j}}{(N-1)}} \tag{3.3}$$

where $\overline{s}$ is the expected value (the weighted mean):

$$\overline{s} = \frac{\sum_{j=1}^{N} \frac{s_j}{W_j}}{\sum \frac{1}{W_j}} \tag{3.4}$$

We can then define a function $\chi_{\rm lim}(\overline{s})$ that decide whether the χ-value for a pixel is acceptable or not. $\chi_{\rm lim}(\overline{s})$ is defined using a σ cut level χ_0, a rejection ceiling C, and a rejection ceiling scaling α in the following way:

$$\chi_{\rm lim}(\overline{s}) = \begin{cases} \chi_0 & \text{if } \overline{s} < C\sigma_{sky} \\ \alpha \frac{\overline{s}}{\sigma_{sky}} + \beta & \text{if } \overline{s} > C\sigma_{sky} \end{cases} \tag{3.5}$$

Here β can be found from the condition that $\chi_{\rm lim}(\overline{s})$ should be continuous in $\overline{s}$: $\beta = \chi_0 - \alpha C$. Finally, I combined the stacked data from the old and the new CCD by measuring the SN ratio in both stacked images. The final image is the weighted sum of the two stacked images with the largest weight of 75% put on the stack from the new CCD, since the SN ratio is so much better for new improved double CCD in blue wavelength range. However, I needed to use Geotran to make the two image stacks fit together on top of each other.

3.3 Magnitude zero point from spectrophotometric standard stars

In order to calculate the AB magnitudes and luminosity of the 18 LAEs we need to find the magnitude zero point of the combined $NB_{\rm LyC}$ image. What we need to do is to use an image of spectrophotometric standard star, which SED is known and compare with a science image taken on the same night. However, we are going to go through the following steps for more than just one standard star image, to have more nights to choose from. I checked the Paranal weather database to avoid using images taken at nighttimes with clouds. I only use images from observation nights with no cloud coverage on time of observation or no cloud coverage at all, during the night. Using the SED we can find what magnitudes the standard star should have observed through the $NB_{\rm LyC}$ filter. We can then measure the observed flux from the standard star in the image and find the magnitude zero point on that particular night. However, we need to correct for the atmospheric extinction.

Let us start by finding the AB magnitudes of spectrophotometric standard stars. We can model the $NB_{\rm LyC}$ filter profile using a gaussian function centered on the filter center wavelength, $\lambda = 3717$ Å and having a filter width of FWHM = 73 Å. The model-filter profile will then be:

$$\exp\Big(-\frac{(x-3717)^2}{2\sigma^2}\Big) \tag{3.6}$$

where x is in units of Angstrom and we get σ using the FWHM and the relation:

$$\begin{aligned} \mathrm{FWHM} &= 2\sigma\sqrt{2\ln 2} \Leftrightarrow \\ \sigma &= \frac{\mathrm{FWHM}}{\sqrt{8\ln 2}} = \frac{73}{\sqrt{8\ln 2}} \end{aligned} \tag{3.7}$$

The gaussian function used to model the $NB_{\rm LyC}$ -filter can be seen in figure 3.2. We do not bother about getting the peak transmission of the filter right. *Why*? Because we are observing both the standard stars and the LAEs using the same filter. From a mathematical point of view, this means that we would just have to multiply the model with a constant and this will go outside the integral in both denominator and nominator in (3.8) below, and cancel out anyway. I have used absolute SED data from ESO's official list of FORS1 spectroscopic standard stars (http://www.astrossp.unam.mx/setandar/standrads/FORS1_Std.html). The data file for the star Feige 67 (Oke, 1990) contain the average AB magnitudes of small wavelength bins, using a bin size of 7 Å for wavelength $\leq$ 4700 Å and a bin size of 13 Å for wavelength $>$ 4700 Å. Figure 3.3 shows the absolute SED for the star Feige 67 on the interval from 3200 Å to 4200 Å. The absolute SED for the other standard stars are obtained in a similar way, but using a bin size of 50 Å (Hamuy et al., 1994).

We can use a spline to interpolate between data points and obtain an integrable absolute SED function, $F_{\rm AB}(\lambda)$, for each standard star, on the wavelength interval from 3200 to 4200 Å. We can now get the absolute magnitude in the AB-system, by performing the calculation for each star:

$$\mathrm{AB} = \frac{\int_{3200}^{4200} F_{\rm AB}(\lambda)\exp\Big(-\frac{(\lambda-3717)^2}{2\sigma^2}\Big)d\lambda}{\int_{3200}^{4200}\exp\Big(-\frac{(\lambda-3717)^2}{2\sigma^2}\Big)d\lambda} \tag{3.8}$$

The calculated AB magnitudes are shown in the third column of table 3.1 and 3.2 below. We can find the atmospheric extinction in a similar way. I assume that the

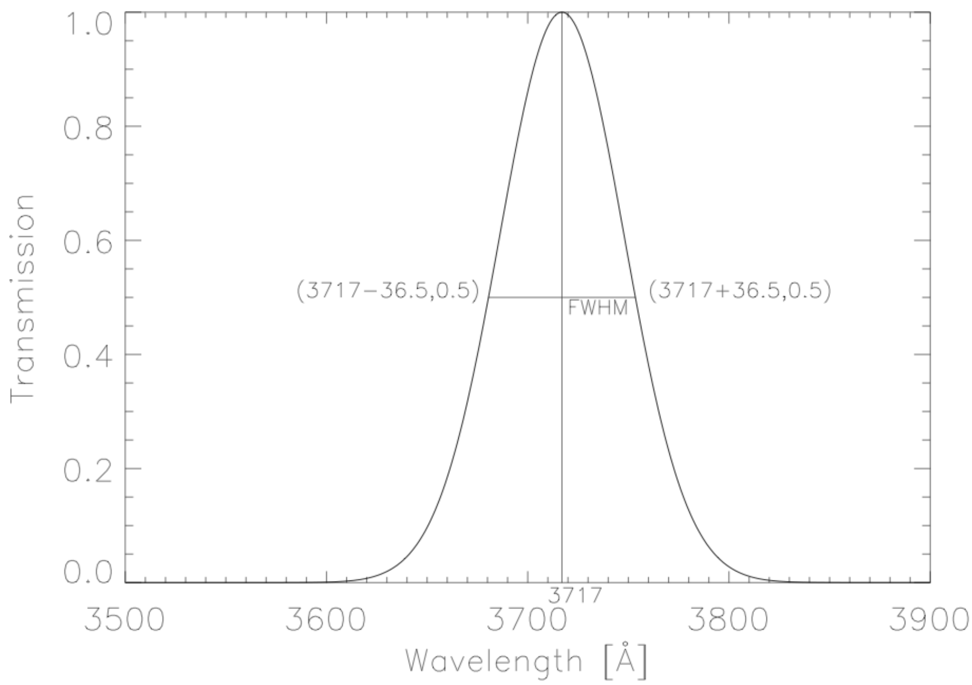

Figure 3.2: The gaussian function that is used to model the NB_{LyC} -filter. The units of the transmission are arbitrary.

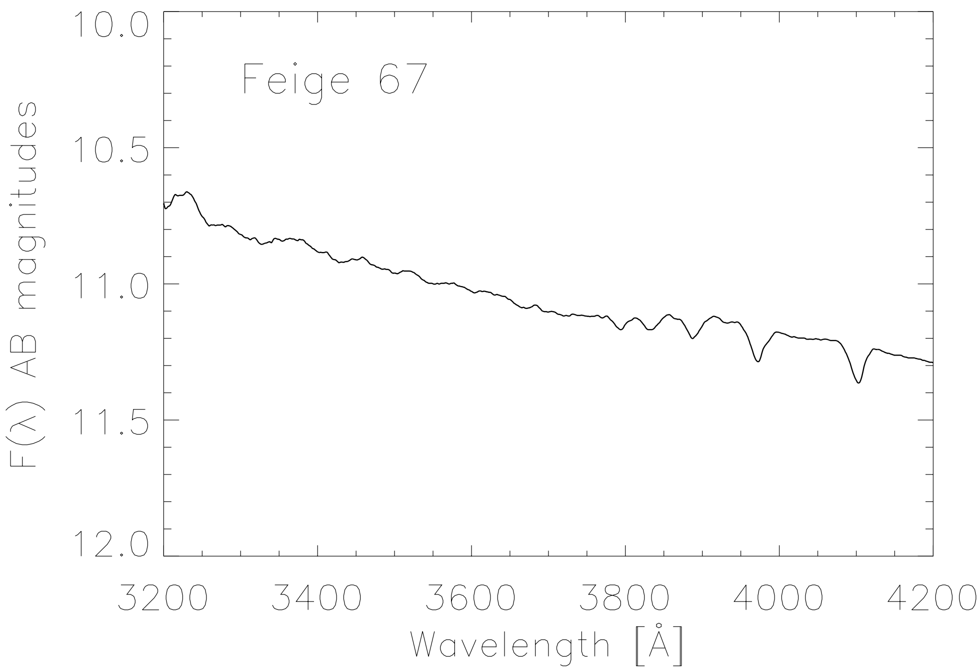

Figure 3.3: The absolute SED of the spectrophotometric standard star, Feige 67, on the interval from 3200 Å to 4200 Å. The distribution is in AB magnitudes as a function of wavelength in Angstrom. This is a discrete distribution from Oke (1990).

Star	Obs. night	AB	Flux	Exp. time	Airmass	m_0
LLT 7987	2006-04-24	12.4161	18927.19	0.9995	1.01100	23.51
Feige 67	2006-07-18	11.1069	1014117.0	19.9995	1.49700	23.47
LLT 4816	2006-07-20	14.0215	228701.8	59.9956	1.21300	23.46

Table 3.1: Input/output data to equation (3.9) and calculated zero points for each image from the old CCD.

Star	Obs. night	AB	Flux	Exp. time	Airmass	m_0
LTT 3218	2007-04-22	12.2334	63423.16	1.9978	1.01200	23.89
LTT 377	2007-07-11	12.2882	316886.7	10.0000	1.01200	23.94
LTT 377	2007-07-12	12.2882	317323.2	9.9999	1.01400	23.95
LTT 6248	2008-03-02	12.7367	374257.2	19.9975	1.02700	23.83
LTT 6248	2008-03-02	12.7367	655137.2	35.0014	1.02600	23.83
LTT 4816	2008-03-03	14.0215	105974.2	19.9981	1.24500	23.83
LTT 6248	2008-03-05	12.7367	380849.6	20.0003	1.00300	23.84
LTT 6248	2008-03-06	12.7367	381493.2	19.9941	1.00500	23.84

Table 3.2: Input/output data to equation (3.9) and calculated zero points for each image from the new CCD, chip 1.

extinction at the Roque de Los Muchachos observatory at La Palma, Canarie Islands is the same as on Mount Paranal in Chile. We can therefore use data of the atmospheric extinction at La Palma obtain by the Isaac Newton Group of Telescopes. The approach is basically the same as for calculating the absolute magnitudes of the standard stars above. The extinction data is in units of magnitudes per airmass and I need to find the bandpass per airmass through the NB_{LyC} -filter. Again I use a spline to interpolate between the data points and get a integrable function $E_{\mathrm{AB}}(\lambda)$, that model the extinction per airmass as a function of wavelength on the interval from 3200 to 4200 Å. I find that the extinction is 0.40 in units of magnitudes/airmass. Now we have to measure the standard stars flux counts in each images. I used the ESO software MIDAS to measure flux from the standard stars (http://WWW.eso.org/sci/data-processing/software/esomidas/). I used a 50 pixel diameter circular aperture to measure the flux. The measured flux counts are list in table 3.1 and 3.2 below. We are now ready to find the magnitude zero points m_0, for the different nights of observations using the expression:

$$m_0 = \mathrm{AB} + 2.5\log\left(\frac{\mathrm{Flux}}{\mathrm{Exp.\ time}}\right) + \mathrm{Extinction/airmass} \times \mathrm{Airmass} \tag{3.9}$$

The calculated zero points are listed in the last column of table 3.1 and 3.2. They are very stable for each chip. Their are of cause a difference between the new and the old CCD. I have not calculated the zero point for the new chip2, since I will only have to use one of the zero points in the next step. The next step is to find the magnitude of a star in one of the science frames using the corresponding m_0 measured on the same night. I choose a science frame taken on the night of Marts 6, 2008. The zero point for this night is 23.84 AB, as can be seen from the last row of table 3.2. Using this zero point, I find the magnitude of the star is:

$$\begin{aligned} AB &= m_0 - 2.5\log\left(\frac{\text{star flux count}}{\text{exp. time}}\right) - (\text{extinction/airmass}) \times \text{airmass} \\ &= 23.8388 - 2.5\log\left(\frac{21138.14}{1599.9377}\right) - 0.398683 \times 1.21700 \\ &= 20.55 \end{aligned} \tag{3.10}$$

Now that we know what the magnitude of the this star is, we can find the same star in the combined image and since we already know what the magnitude should be for this star, we can determine what the zero point m_0 is, in the combined image. Doing this, I find that m_0 for the combined image to be:

$$m_0 = 20.5512 + 2.5\log(16585.94) = 31.10 \tag{3.11}$$

This is the magnitude zero point we need, when we in the next chapter start on doing the real photometry and measure how much LyC flux are reaching us from the 18 LAE. However, what we have found here is m_0 measured using a 50 pixel aperture, when measuring the LyC we will use a smaller 10 pixel aperture and correct for the difference. I find that their is factor of 1.36 between the flux measured in the two apertures.

Chapter 4

Photometry and Escape Fractions

In this chapter I will use my newly found magnitude zero point for the combined image to find the AB magnitudes in the $NB_{\rm LyC}$ band image, of my sample LAEs. I will use these magnitudes together with the magnitudes from Grove et al. (2009) to calculate the luminosity densities and SED for each of LAEs. Finally I will define and estimate the relative escape fractions of ionizing photons, but let me start this chapter by the photometric measurements that will reveal how many of the LAE we can detect in LyC, if any.

4.0.1 Photometric measurements

After all the calibration and data reduction, I am now finally ready to measure how much Lyman continuum flux we can observe, from the LAEs. First I cut out smaller sub-images centered on the LAEs. I made a sample of sub images from both the LyC and Lyα images. It was necessary to make cutouts because, it was not possible to align the two full images on top of each other in such a way that all 18 LAEs were exactly on top of each other - some part of the images seem to have a small shift (few pixel) compared to the other, due to distortion. The size of the cutouts, (300×300 pixel), was chosen so that it was possible to use other objects that is visible in both narrow-band images to align them perfectly on top of each other. It was also important that the LyC sub images were large enough to make it possible to measure the variance of the local sky background around the LAE.

I used the ESO software MIDAS to do the actual measurement on the $\rm NB_{LyC}$ sub-images by going through the following steps:

1. Loading the $\rm NB_{Ly\alpha}$ sub-image into the MIDAS window, then put a 10 pixel diameter aperture mark around the position of the LAE Lyα emission.

2. Loading the corresponding $\rm NB_{LyC}$ sub-image into the same window, exactly on top of the other. The aperture mark was still shown, now on the $\rm NB_{LyC}$ sub-image.

3. I then measured the flux-count inside the aperture mark using the same 10 pixel diameter aperture.

4. Then I estimated the sky background by measuring the background flux-count, using the same aperture, in 15 different areas around the LAE with no visible objects.

5. The measured LyC emission was then obtained by taking the flux-count from the LAE and subtracting the mean sky background flux-count.

6. Finally I calculated the variance of the sky background and from the variance I then obtained the standard deviation, σ, which is what I use as the uncertainty in the measurement.

This procedure was used to measure the LyC emission from all 18 LAEs. I did consider using a larger aperture for some of the LAEs which have extended Laα emission, e.g. LAE id02 and id09, but they also have close neighboring objects. Therefore, I decided to use the 10 pixel diameter aperture for all of the LAEs, trying to avoid contaminating flux from neighboring objects. To check the applied technique for consistency, I did more than one measurement of each object. I find that the standard deviation σ, of a measurement, generally changes by a few percent from one measurement to another. However, for some of the LAE, σ changes up to 30% from one measurement to another of the same LAE. If I move the aperture a few pixels on the LAE I find that the measured LyC flux-count in general changes less that one σ, but some of LAE are more sensitive to where I put the aperture and for those, the measured flux-count will change $\sim 1\sigma$. In table 4.1 measurement of the LyC flux is listed along with σ for each of the 18 LAE and we can see that I only obtain a $> 3\sigma$ detection in three cases: id2, id7 and id8, which I will discuss below. To comparison, Iwata et al. (2009) detect LyC from 10 LAEs out of a sample of 125. Non of the LAEs have negative flux-counts after sky-subtraction. I also tried to stack small stamp images of the 18 LAEs in the NB_{LyC} using the median, to investigate if I could see any flux in the median image. However, I did not detect anything, using this more statistical approach.

4.1 Magnitudes Calculation

Before I could use the magnitude zero point obtained in section 3.3, I had to correct for the different size in aperture used in measurement of the standard star and the LAE. In order to find the appropriate correction factor, I measure several different sources in the NB_{LyC} image using both apertures. I find that correction factor should be ~ 1.36. The magnitude zero point we have from (3.11) is $m_0 = 31.10$. From the Extinction Calculator at the home page of the NASA/IPAC Extragalactic Database (http://nedwww.ipac.caltech.edu/forms/calculator.html), I find that the Galactic extinction in the direction of BRI1202-0725. I use the following magnitude

id	Flux count (σ)	$\mathrm{NB_{LyC}}$	$\mathrm{NB_{Ly\alpha}}$	V	R
1	21.34 (11.654)	≥ 27.15	$24.18^{+0.10}_{-0.09}$	$24.93^{+0.10}_{-0.09}$	$24.88^{+0.11}_{-0.10}$
2	86.73 (12.950)	$25.73^{+0.18}_{-0.15}$	$22.06^{+0.01}_{-0.01}$	$23.31^{+0.02}_{-0.02}$	$23.53^{+0.03}_{-0.03}$
3	12.58 (10.472)	≥ 27.27	$26.32^{+0.34}_{-0.26}$	$27.24^{+0.42}_{-0.30}$	$27.71^{+0.88}_{-0.48}$
4	8.212 (14.706)	≥ 26.90	$23.12^{+0.03}_{-0.03}$	$24.50^{+0.05}_{-0.05}$	$24.97^{+0.09}_{-0.08}$
5	4.737 (9.6133)	≥ 27.36	$25.12^{+0.19}_{-0.16}$	$25.80^{+0.18}_{-0.15}$	$26.11^{+0.28}_{-0.22}$
6	25.57 (12.862)	≥ 27.04	$25.54^{+0.23}_{-0.19}$	$26.81^{+0.41}_{-0.30}$	≥ 27.95
7	58.11 (11.171)	$26.16^{+0.23}_{-0.19}$	$25.71^{+0.24}_{-0.19}$	$26.33^{+0.21}_{-0.18}$	$26.29^{+0.23}_{-0.19}$
8	38.14 (11.947)	$26.62^{+0.41}_{-0.30}$	$25.19^{+0.18}_{-0.16}$	$26.49^{+0.26}_{-0.20}$	$26.18^{+0.28}_{-0.22}$
9	14.06 (8.986)	≥ 27.43	$23.12^{+0.05}_{-0.05}$	$24.25^{+0.07}_{-0.07}$	$24.56^{+0.11}_{-0.10}$
10	4.110 (10.864)	≥ 27.23	$24.68^{+0.07}_{-0.07}$	$26.65^{+0.25}_{-0.20}$	$27.47^{+0.74}_{-0.44}$
11	24.49 (11.136)	$27.10^{+0.66}_{-0.41}$	$24.78^{+0.12}_{-0.11}$	≥ 27.96	≥ 27.83
12	23.19 (10.999)	$27.16^{+0.70}_{-0.42}$	$25.71^{+0.19}_{-0.16}$	$27.56^{+0.65}_{-0.41}$	$28.02^{+1.63}_{-0.62}$
13	21.26 (10.056)	$27.25^{+0.70}_{-0.42}$	$25.67^{+0.22}_{-0.19}$	≥ 28.22	≥ 28.09
14	9.986 (8.9464)	≥ 27.44	$25.11^{+0.17}_{-0.15}$	≥ 27.91	≥ 27.78
15	14.61 (10.248)	≥ 27.29	$25.43^{+0.16}_{-0.14}$	≥ 28.32	≥ 28.19
16	22.10 (14.809)	≥ 26.89	$25.57^{+0.21}_{-0.17}$	$27.44^{+0.74}_{-0.44}$	$26.15^{+0.20}_{-0.17}$
17	23.47 (10.683)	$27.14^{+0.66}_{-0.41}$	$25.52^{+0.15}_{-0.13}$	$27.74^{+0.76}_{-0.44}$	$28.07^{+1.59}_{-0.62}$
18	12.85 (11.617)	≥ 27.16	$25.78^{+0.29}_{-0.232}$	≥ 28.10	≥ 27.97

Table 4.1: The first column shows the flux count measured in the NB_{LyC} image and associated standard deviation σ, of the measurement. Column 2 list the calculated NB_{LyC} AB magnitudes. I have used 2σ to find a lower bound of magnitude for LAEs that have a measured flux count lower than 2σ. Column 3-5 list the AB magnitudes from Grove et al. (2009). All magnitudes are corrected for Galactic extinction.

corrections in the four bands: $NB_{\mathrm{LyC}} = 0.200$, $NB_{\mathrm{Ly\alpha}} = 0.130$, $V = 0.122$ and $R = 0.098$. It is now easy to calculate the magnitudes in the $\mathrm{NB_{LyC}}$-filter image using:

$$\mathrm{AB} = 31.10 - 2.5 \times \log(1.36 \times \text{measured flux}) - 0.20 \tag{4.1}$$

For the LAE which has a measured LyC flux less than 2σ I have used 2σ as an upper boundary for the LyC flux which then give a lower boundary for magnitude. For LAE which has a LyC flux Larger than 2σ, I have used the measured flux to calculate the AB magnitude and $\pm\sigma$ as the error in the measured flux. This is then transform into an upper and lower uncertainty in the AB magnitudes. The results are given in table 4.1. For completion I also list the AB magnitudes in the $\mathrm{NB_{Ly\alpha}}$, V and R bands taken from Grove et al. (2009) and corrected for Galactic extinction.

4.2 Specific Flux and Luminosity Density

I calculate the specific flux f_ν, using the AB magnitudes from table 4.1 and rewriting the relation between f_ν and the apparent AB magnitude (Oke, 1974):

$$\begin{aligned} AB &= -2.5 \log f_\nu - 48.6 \\ f_\nu &= 10^{-0.4(\mathrm{AB}+48.6)} \end{aligned} \tag{4.2}$$

The units of the specific flux is erg s^{-1} Hz^{-1} cm^{-2}. The next step is to find the luminosity density. Using the Cosmological Calculator at http://www.astro.ucla.edu/-~wright/CosmoCalc.html, I find the luminosity distance to an object at redshift $z = 3.2$, to be $d_L = 8.47513 \times 10^{28}$ cm, assuming a flat Λ-dominated cosmology with $\Omega_\Lambda = 0.7$ and $\Omega_\mathrm{m} = 0.3$, and the current Hubble constant to be $H_0 = 70$ km s^{-1}. From the specific flux and the luminosity distance I can find the luminosity which has units of erg s^{-1} Hz-1:

$$L = \frac{4\pi f_\nu d_l^2}{1+z} \tag{4.3}$$

The luminosity in the four filter-bands for all 18 LAEs, is listed in table 4.2. I have plotted the luminosity of each of the 4 filters against the central wavelength of each filter. This gives a crude SED for each of 18 LAE based on the two narrow-band and the two broad-band filters. Figure 4.1 to 4.18 shows the SED for each the 18 LAEs, together with 17×17 arcsec^2 stamp images of the LAE in each band. In the cases where the measured LyC flux-count are less than two 2σ, I have used 2σ to calculate an upper limit for the luminosity.

id	$L(\text{LyC})$ 10^{27} erg s^{-1} Hz^{-1}	$L(\text{Ly}\alpha)$ 10^{28} erg s^{-1} Hz^{-1}	$L(V)$ 10^{27} erg s^{-1} Hz^{-1}	$L(R)$ 10^{27} erg s^{-1} Hz^{-1}
1	< 10.75	16.61 ± 1.46	83.38 ± 7.34	86.99 ± 8.39
2	40.01 ± 5.97	117.02 ± 1.08	370.73 ± 6.89	301.62 ± 8.45
3	< 9.66	2.31 ± 0.63	9.93 ± 3.19	6.42 ± 3.57
4	< 13.57	44.08 ± 1.24	123.90 ± 5.84	80.07 ± 6.37
5	< 8.87	6.99 ± 1.12	37.42 ± 5.72	28.02 ± 6.37
6	< 11.87	4.75 ± 0.91	14.76 ± 4.70	< 5.15
7	26.81 ± 5.15	4.06 ± 0.80	22.97 ± 4.14	23.74 ± 4.53
8	17.59 ± 5.51	6.55 ± 1.00	19.82 ± 4.22	26.27 ± 5.97
9	< 8.29	44.08 ± 2.08	155.97 ± 10.39	116.80 ± 11.27
10	< 10.02	10.48 ± 0.70	17.10 ± 3.52	8.01 ± 4.00
11	11.30 ± 5.14	9.56 ± 1.02	< 5.12	< 5.75
12	10.70 ± 5.07	4.06 ± 0.65	7.40 ± 3.39	4.82 ± 3.75
13	9.81 ± 4.64	4.21 ± 0.81	< 4.03	< 4.52
14	< 8.25	7.05 ± 1.04	< 5.36	< 6.02
15	< 9.45	5.25 ± 0.72	< 3.67	< 4.13
16	< 13.66	4.62 ± 0.81	8.26 ± 4.13	27.01 ± 4.58
17	10.83 ± 4.93	4.83 ± 0.62	6.27 ± 3.15	4.61 ± 3.55
18	< 10.72	3.80 ± 0.90	< 4.50	< 5.05

Table 4.2: The calculated luminosity in the 4 bands. In the NB_{LyC} , $V$and R band, the units are in 10^{27} erg s^{-1} Hz^{-1}. In the $NB_{\text{Ly}\alpha}$band are the units in 10^{28} erg s^{-1} Hz^{-1}. In the cases where the measured LyC flux-count are less than two 2σ, I have used 2σ to calculate an upper limit for the luminosity density. In other cases use the value measured and take $\pm\sigma$ as the uncertainty.

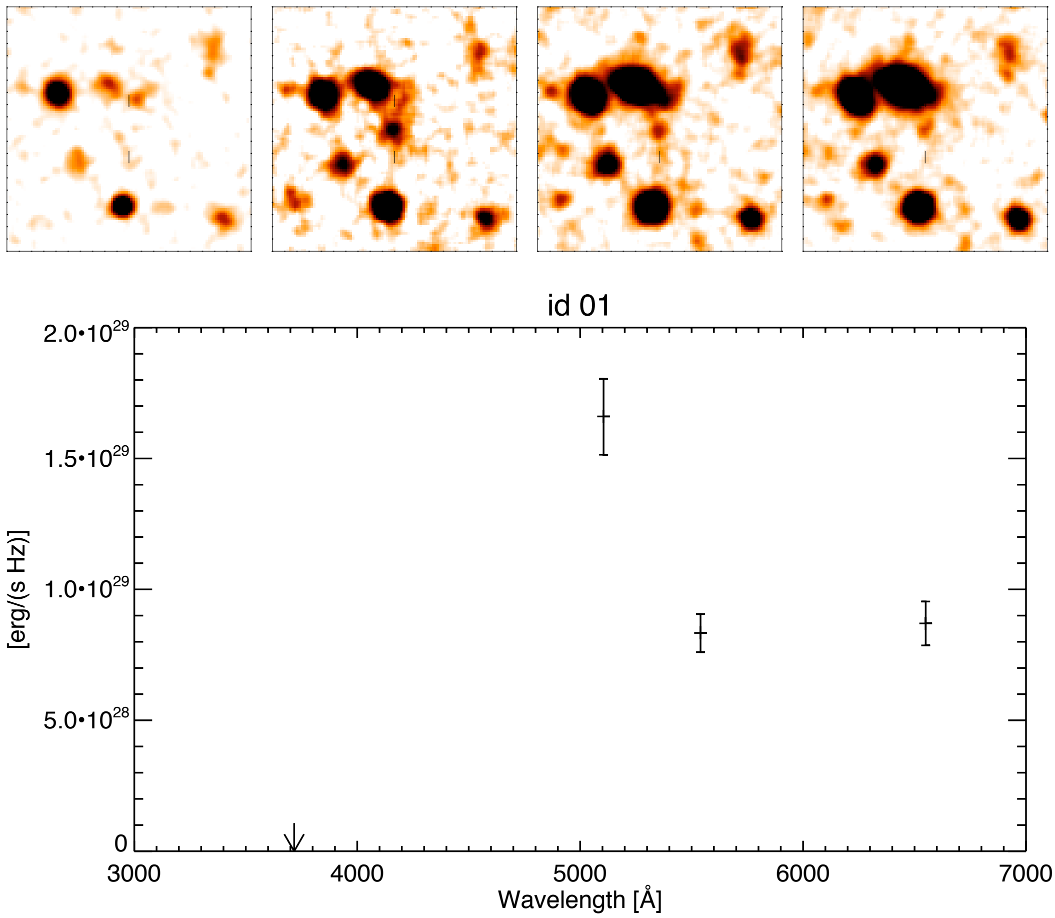

Figure 4.1: 17×17 arcsec^2 images and SED of LAE-id01. Upper part of this figure shows four stamp images of the LAE. From left to right, the four images is in the respective filter-bands: NB_{LyC}, $NB_{\mathrm{Ly}\alpha}$, V and R. The position of the LAE is marked on each image. Lower part of this figure is the SED from the numbers in table 4.2 and the central or effective wavelength of the respective filter-bands.

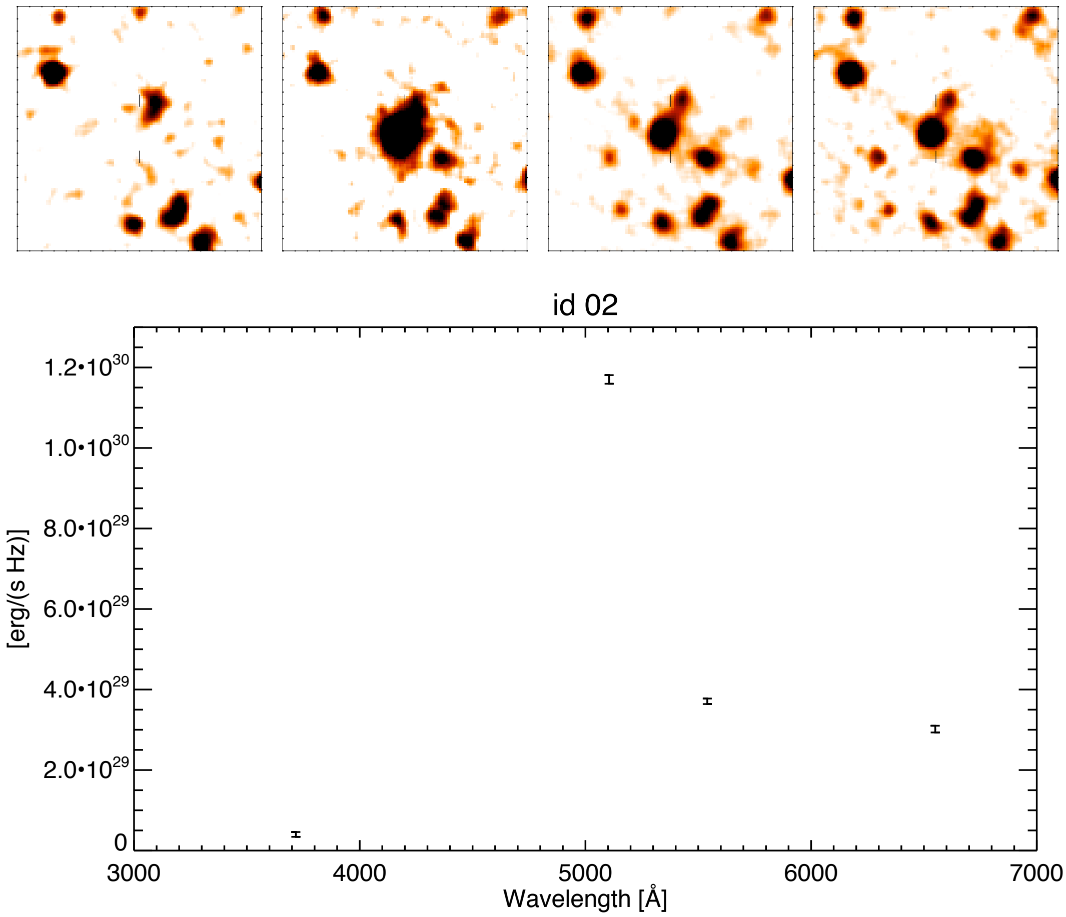

Figure 4.2: 17×17 arcsec^2 images and SED of LAE-id02. Upper part of this figure shows four stamp images of the LAE. From left to right, the four images is in the respective filter-bands: NB_{LyC}, $NB_{\mathrm{Ly}\alpha}$, V and R. The position of the LAE is marked on each image. Lower part of this figure is the SED from the numbers in table 4.2 and the central or effective wavelength of the respective filter-bands. The is the most luminous object in the sample and it is detected in LyC with a strong significant. However, as I discuss in the next chapter, I believe that detection is caused by contamination from the neighboring object.

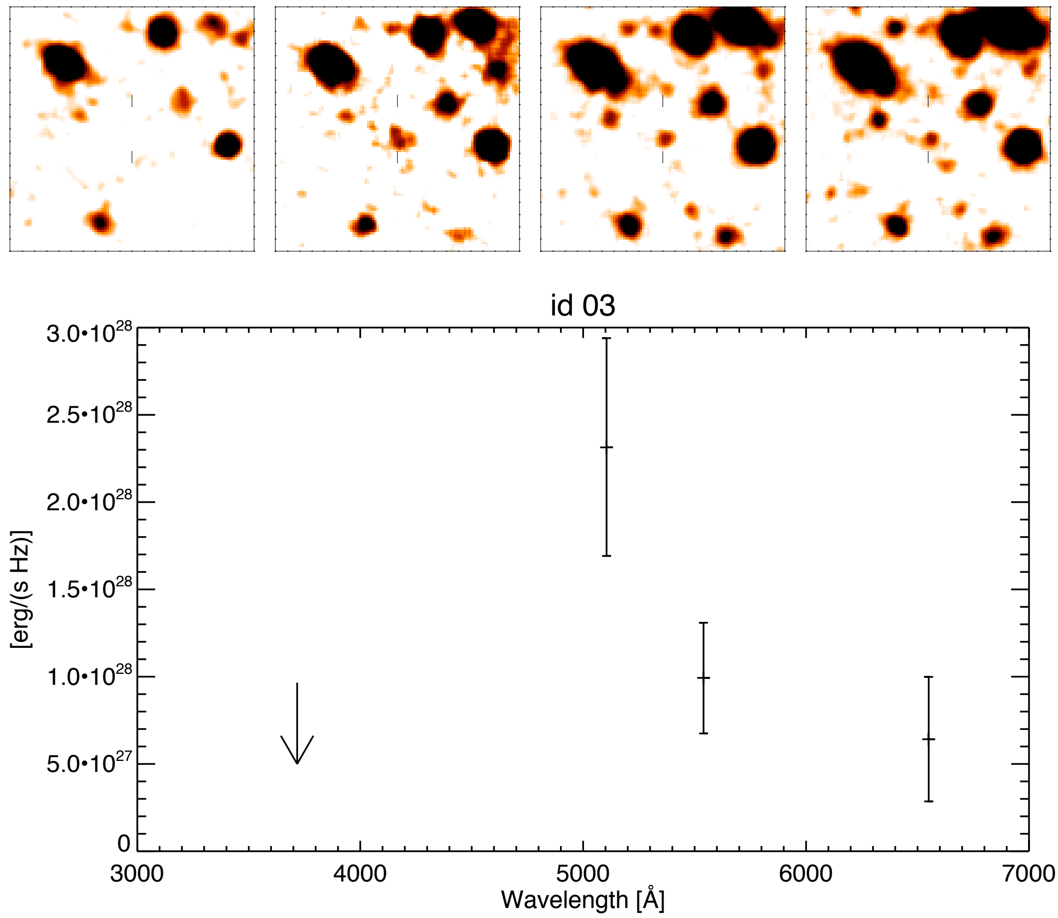

Figure 4.3: 17×17 arcsec^2 images and SED of LAE-id03. Upper part of this figure shows four stamp images of the LAE. From left to right, the four images is in the respective filter-bands: NB_{LyC}, $NB_{\mathrm{Ly}\alpha}$, V and R. The position of the LAE is marked on each image. Lower part of this figure is the SED from the numbers in table 4.2 and the central or effective wavelength of the respective filter-bands.

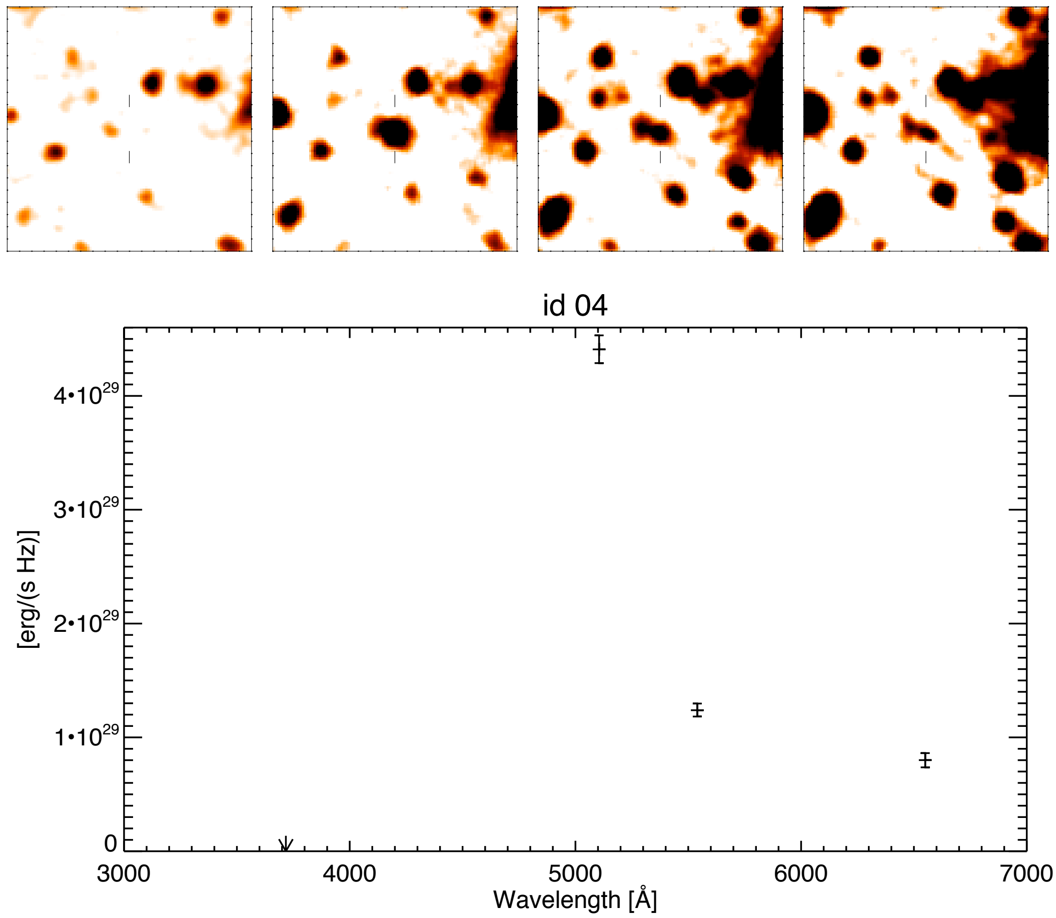

Figure 4.4: 17×17 arcsec^2 images and SED of LAE-id04. Upper part of this figure shows four stamp images of the LAE. From left to right, the four images is in the respective filter-bands: NB_{LyC}, $NB_{\mathrm{Ly}\alpha}$, V and R. The position of the LAE is marked on each image. Lower part of this figure is the SED from the numbers in table 4.2 and the central or effective wavelength of the respective filter-bands.

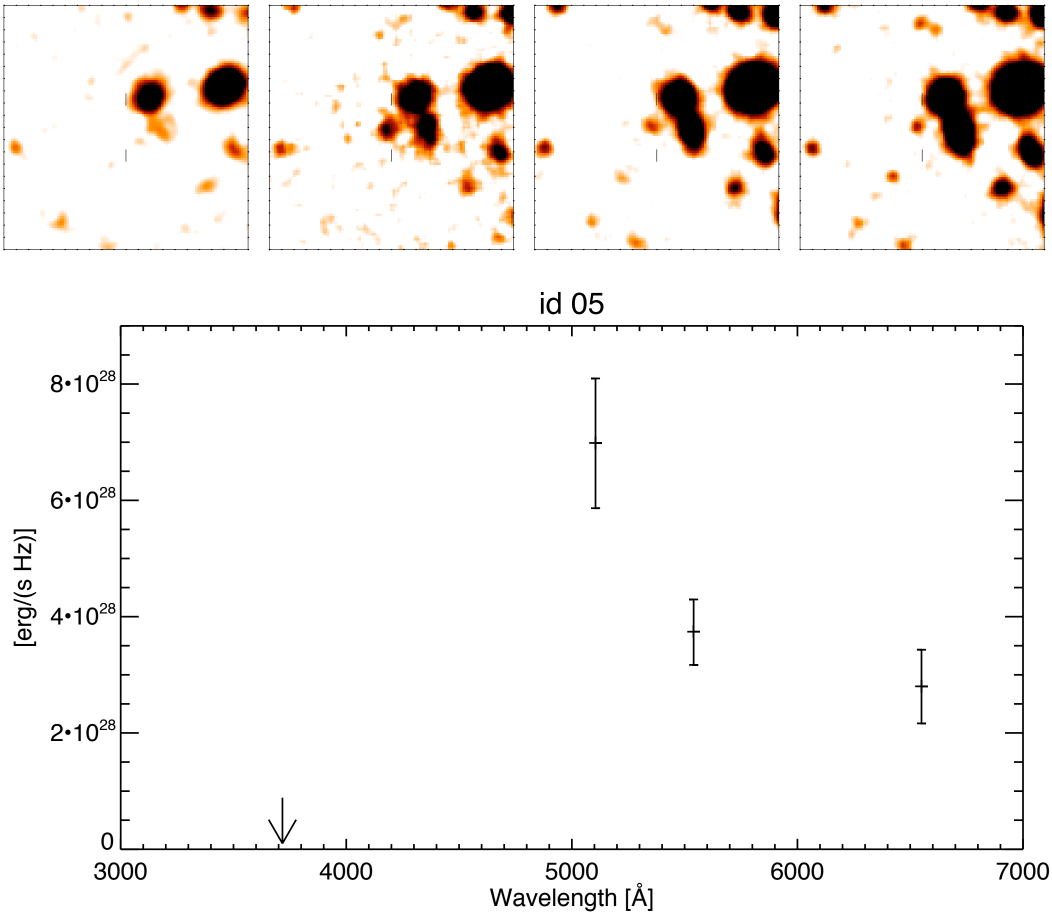

Figure 4.5: 17×17 arcsec^2 images and SED of LAE-id05. Upper part of this figure shows four stamp images of the LAE. From left to right, the four images is in the respective filter-bands: NB_{LyC}, $NB_{\mathrm{Ly}\alpha}$, V and R. The position of the LAE is marked on each image. Lower part of this figure is the SED from the numbers in table 4.2 and the central or effective wavelength of the respective filter-bands.

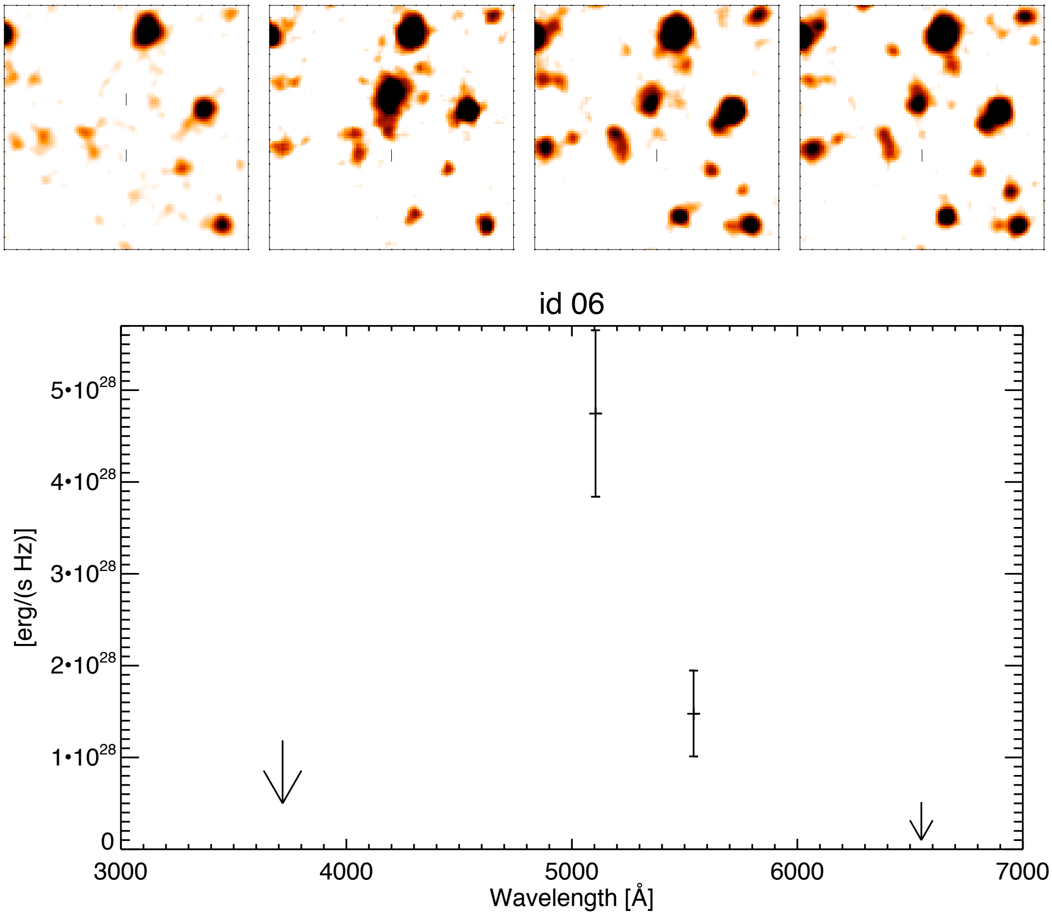

Figure 4.6: 17×17 arcsec^2 images and SED of LAE-id06. Upper part of this figure shows four stamp images of the LAE. From left to right, the four images is in the respective filter-bands: NB_{LyC}, $NB_{\mathrm{Ly}\alpha}$, V and R. The position of the LAE is marked on each image. Lower part of this figure is the SED from the numbers in table 4.2 and the central or effective wavelength of the respective filter-bands.

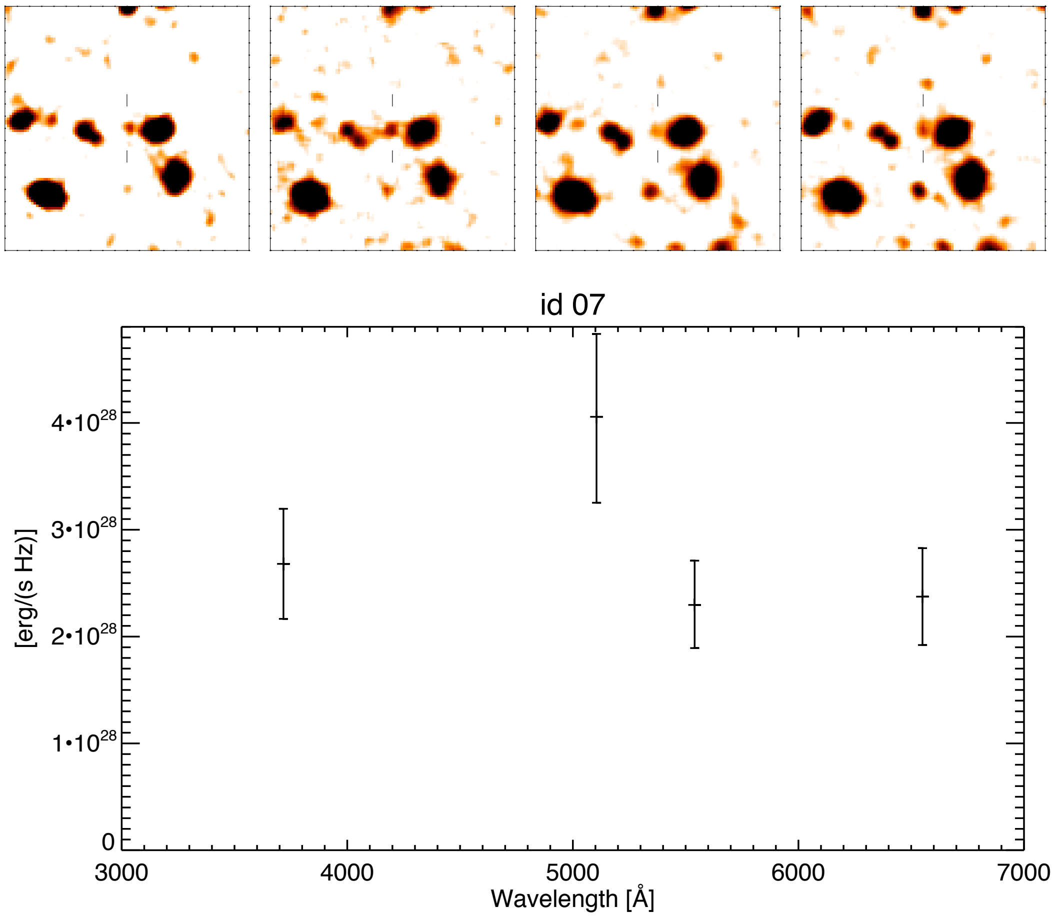

Figure 4.7: 17×17 arcsec^2 images and SED of LAE-id07. Upper part of this figure shows four stamp images of the LAE. From left to right, the four images is in the respective filter-bands: NB_{LyC}, $NB_{\mathrm{Ly}\alpha}$, V and R. The position of the LAE is marked on each image. Lower part of this figure is the SED from the numbers in table 4.2 and the central or effective wavelength of the respective filter-bands. This object is detected in LyC and have a flat constant continuum from the across the Lyα line.

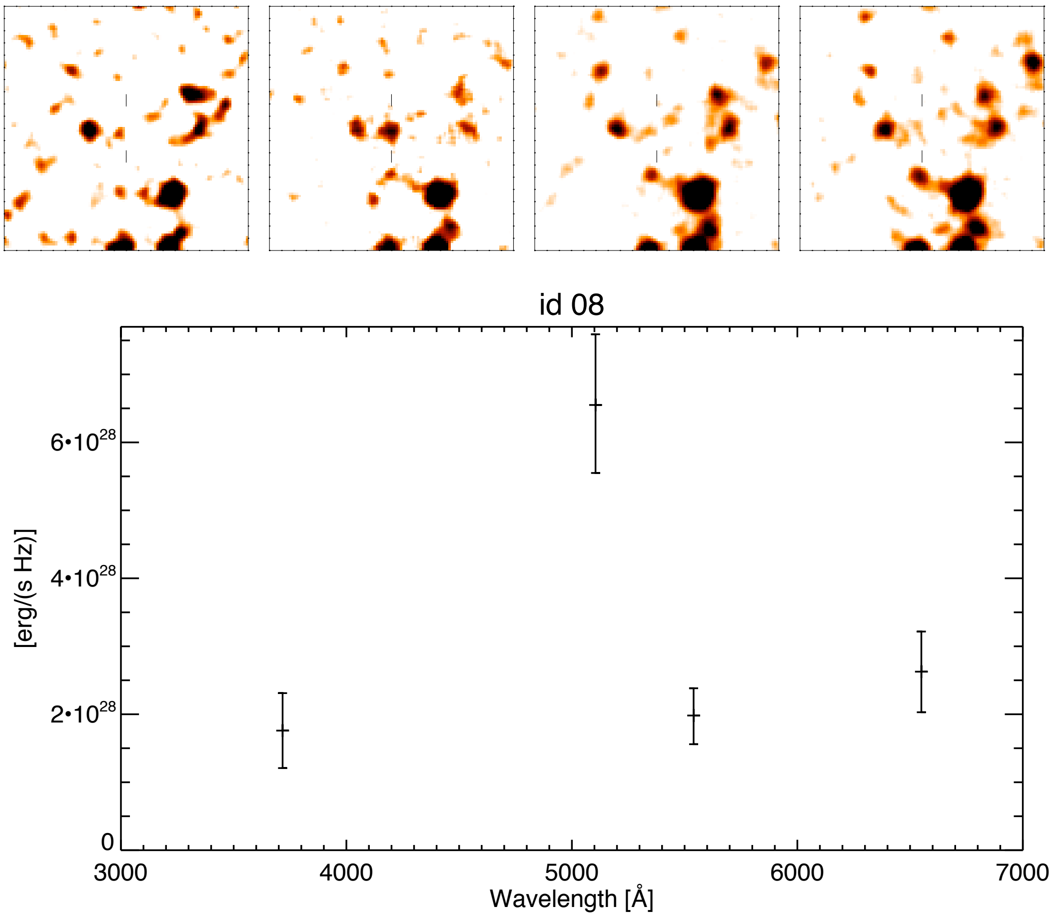

Figure 4.8: 17×17 arcsec^2 images and SED of LAE-id08. Upper part of this figure shows four stamp images of the LAE. From left to right, the four images is in the respective filter-bands: NB_{LyC}, $NB_{\mathrm{Ly}\alpha}$, V and R. The position of the LAE is marked on each image. Lower part of this figure is the SED from the numbers in table 4.2 and the central or effective wavelength of the respective filter-bands. This object is detected in LyC and have a flat constant continuum from the across the Lyα line.

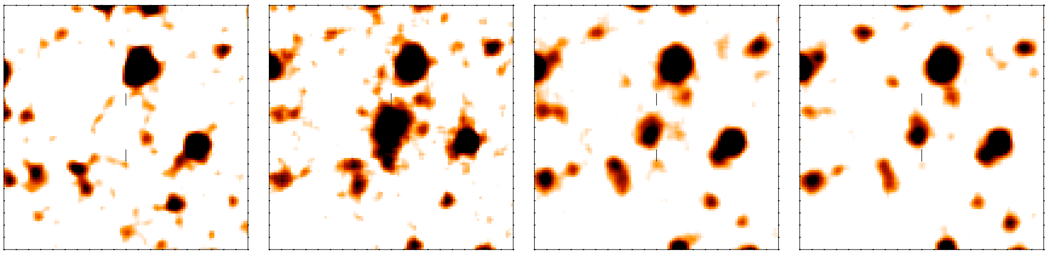

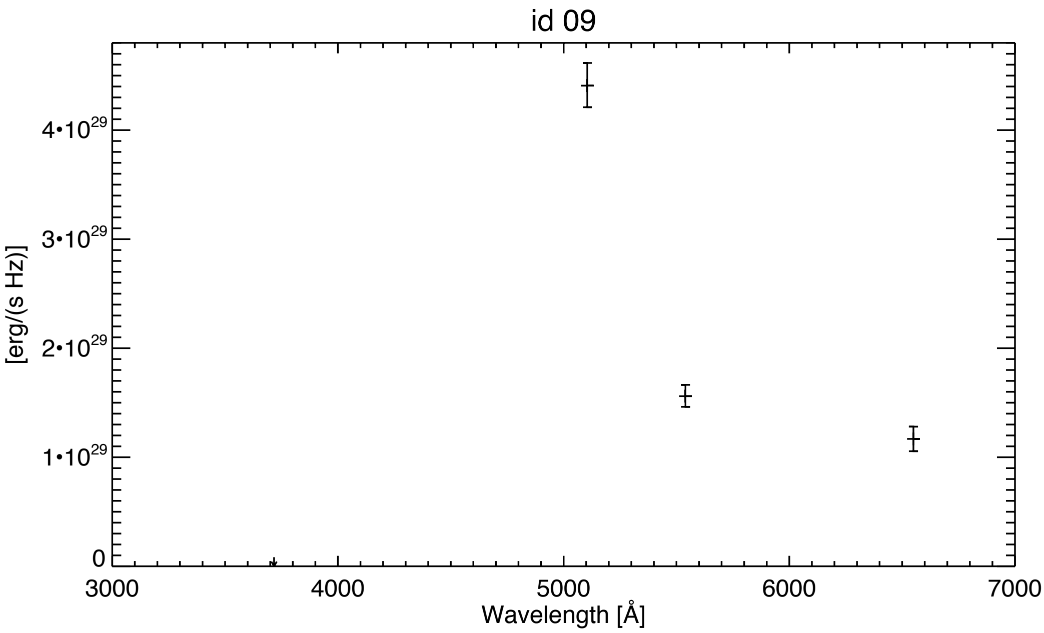

Figure 4.9: 17×17 arcsec^2 images and SED of LAE-id09. Upper part of this figure shows four stamp images of the LAE. From left to right, the four images is in the respective filter-bands: $NB_{\rm LyC}$, $NB_{\rm Ly\alpha}$, V and R. The position of the LAE is marked on each image. Lower part of this figure is the SED from the numbers in table 4.2 and the central or effective wavelength of the respective filter-bands.

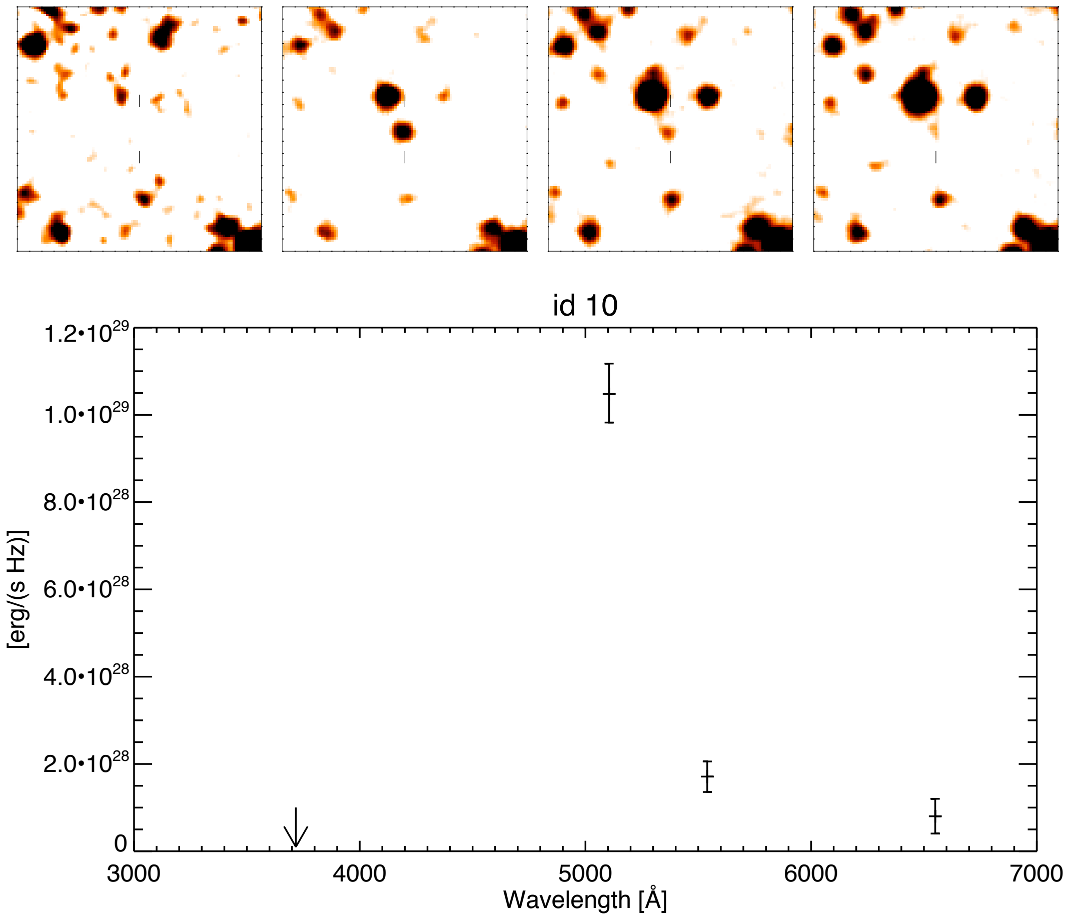

Figure 4.10: 17×17 arcsec^2 images and SED of LAE-id10. Upper part of this figure shows four stamp images of the LAE. From left to right, the four images is in the respective filter-bands: NB_{LyC}, $NB_{\mathrm{Ly}\alpha}$, V and R. The position of the LAE is marked on each image. Lower part of this figure is the SED from the numbers in table 4.2 and the central or effective wavelength of the respective filter-bands.

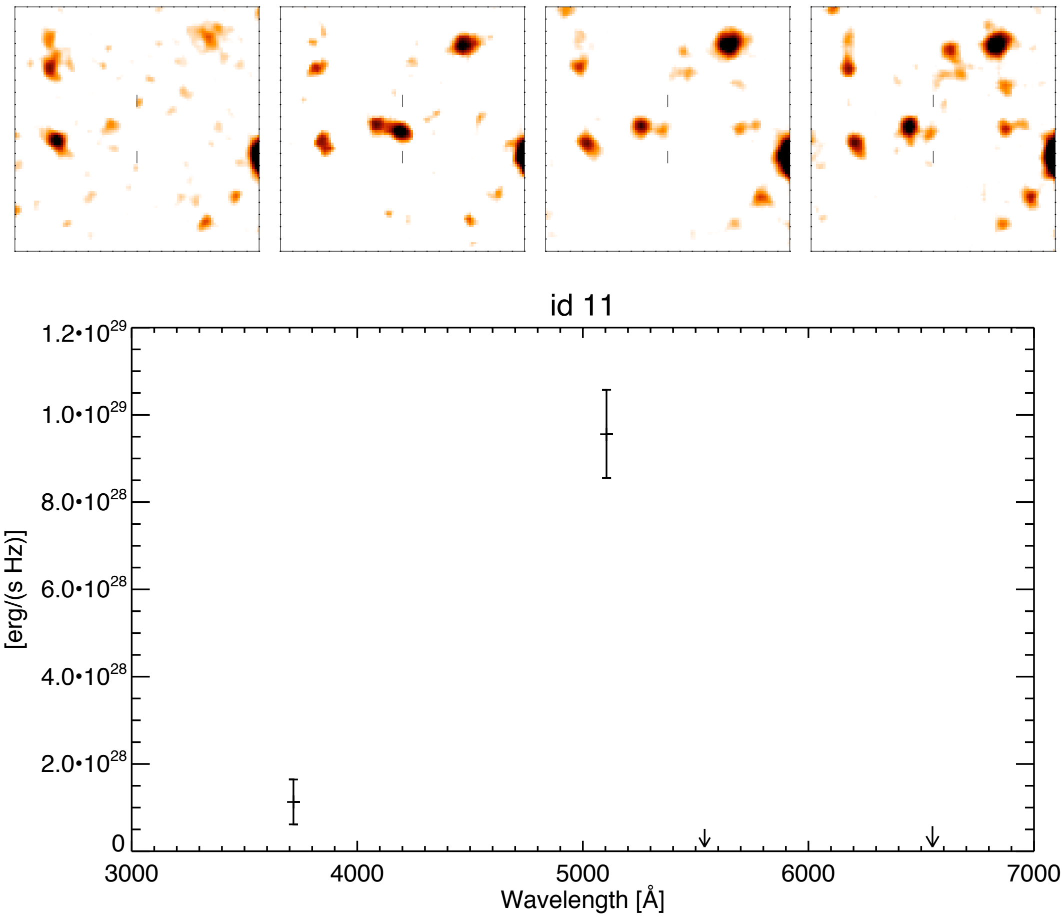

Figure 4.11: 17×17 arcsec^2 images and SED of LAE-id11. Upper part of this figure shows four stamp images of the LAE. From left to right, the four images is in the respective filter-bands: NB_{LyC}, $NB_{\mathrm{Ly}\alpha}$, V and R. The position of the LAE is marked on each image. Lower part of this figure is the SED from the numbers in table 4.2 and the central or effective wavelength of the respective filter-bands.

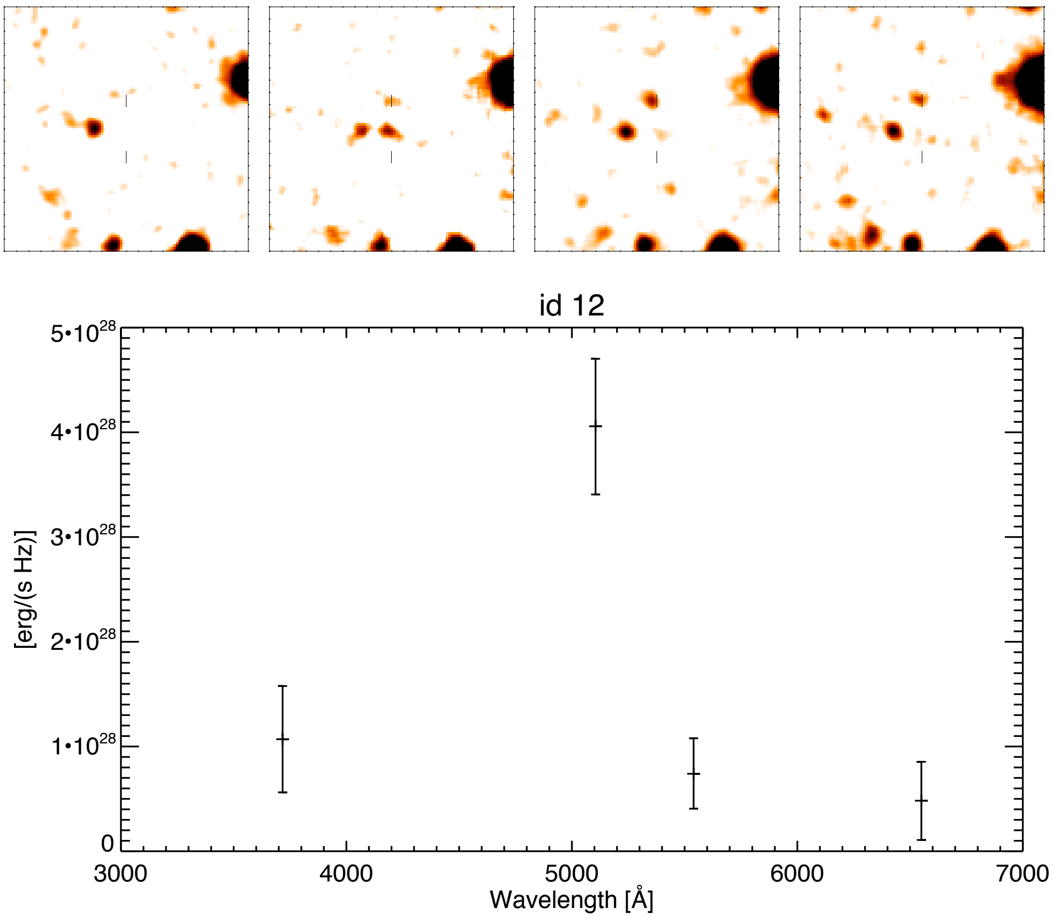

Figure 4.12: 17×17 arcsec^2 images and SED of LAE-id12. Upper part of this figure shows four stamp images of the LAE. From left to right, the four images is in the respective filter-bands: $NB_{\rm LyC}$, $NB_{\rm Ly\alpha}$, V and R. The position of the LAE is marked on each image. Lower part of this figure is the SED from the numbers in table 4.2 and the central or effective wavelength of the respective filter-bands.

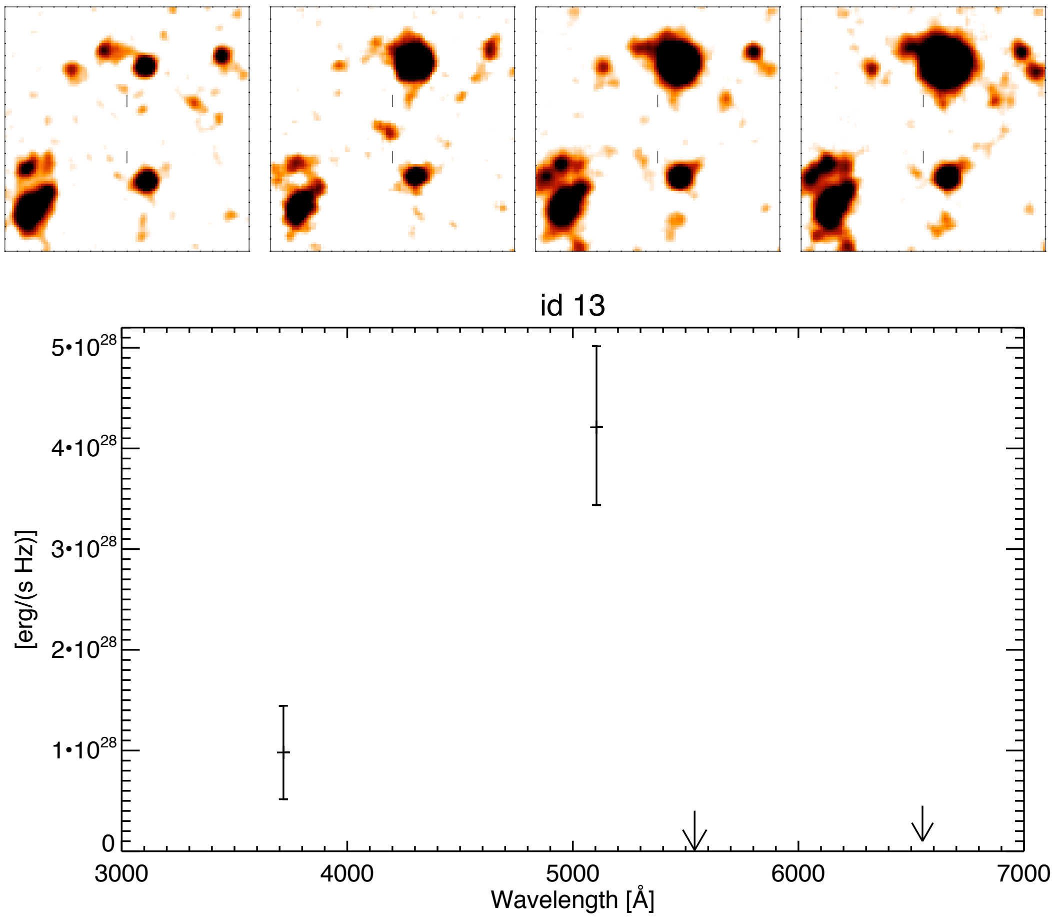

Figure 4.13: 17×17 arcsec^2 images and SED of LAE-id13. Upper part of this figure shows four stamp images of the LAE. From left to right, the four images is in the respective filter-bands: NB_{LyC}, $NB_{\mathrm{Ly}\alpha}$, V and R. The position of the LAE is marked on each image. Lower part of this figure is the SED from the numbers in table 4.2 and the central or effective wavelength of the respective filter-bands.

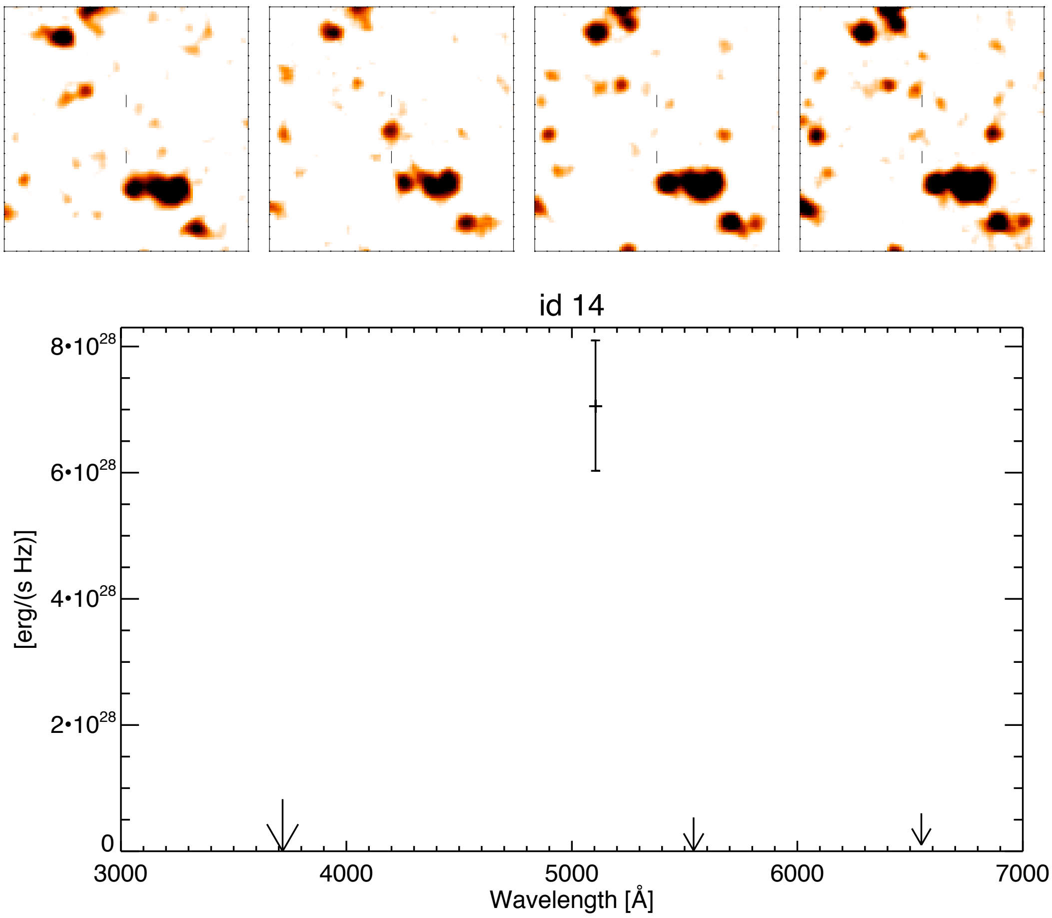

Figure 4.14: 17×17 arcsec^2 images and SED of LAE-id14. Upper part of this figure shows four stamp images of the LAE. From left to right, the four images is in the respective filter-bands: NB_{LyC}, $NB_{\mathrm{Ly}\alpha}$, V and R. The position of the LAE is marked on each image. Lower part of this figure is the SED from the numbers in table 4.2 and the central or effective wavelength of the respective filter-bands.

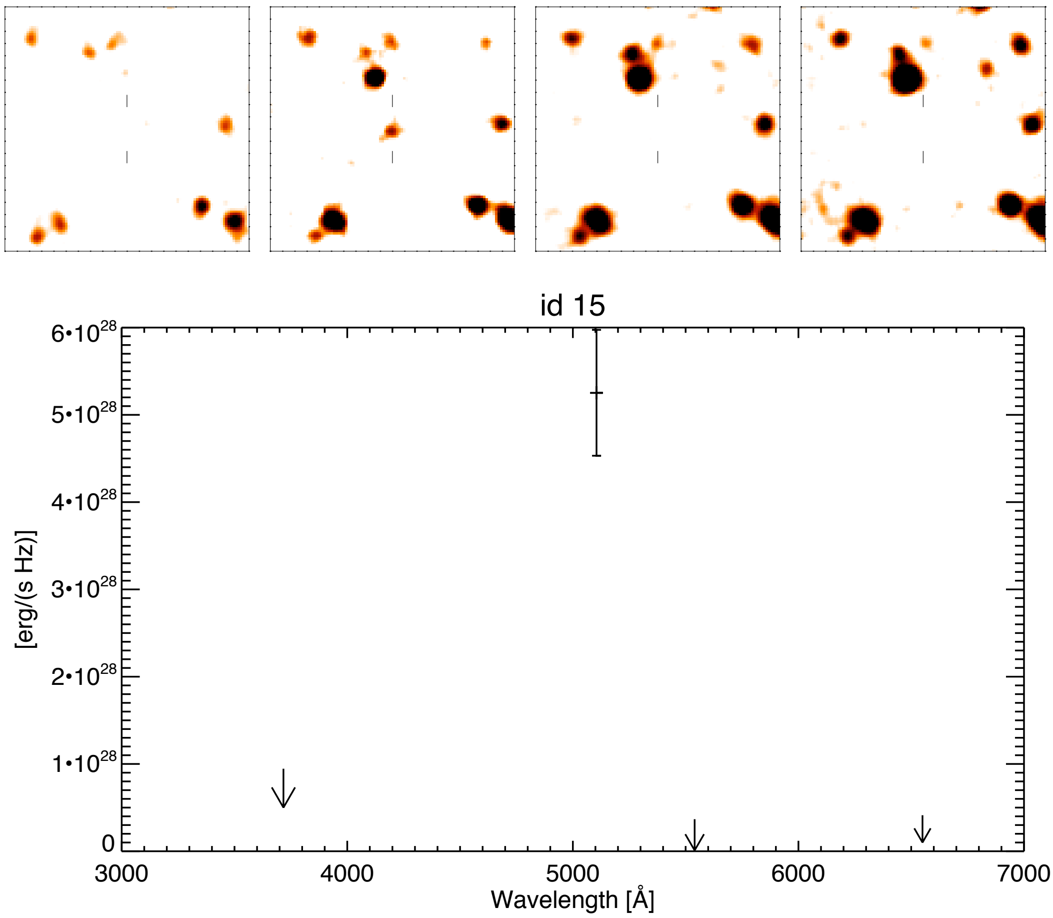

Figure 4.15: 17×17 arcsec^2 images and SED of LAE-id15. Upper part of this figure shows four stamp images of the LAE. From left to right, the four images is in the respective filter-bands: NB_{LyC}, $NB_{\mathrm{Ly}\alpha}$, V and R. The position of the LAE is marked on each image. Lower part of this figure is the SED from the numbers in table 4.2 and the central or effective wavelength of the respective filter-bands.

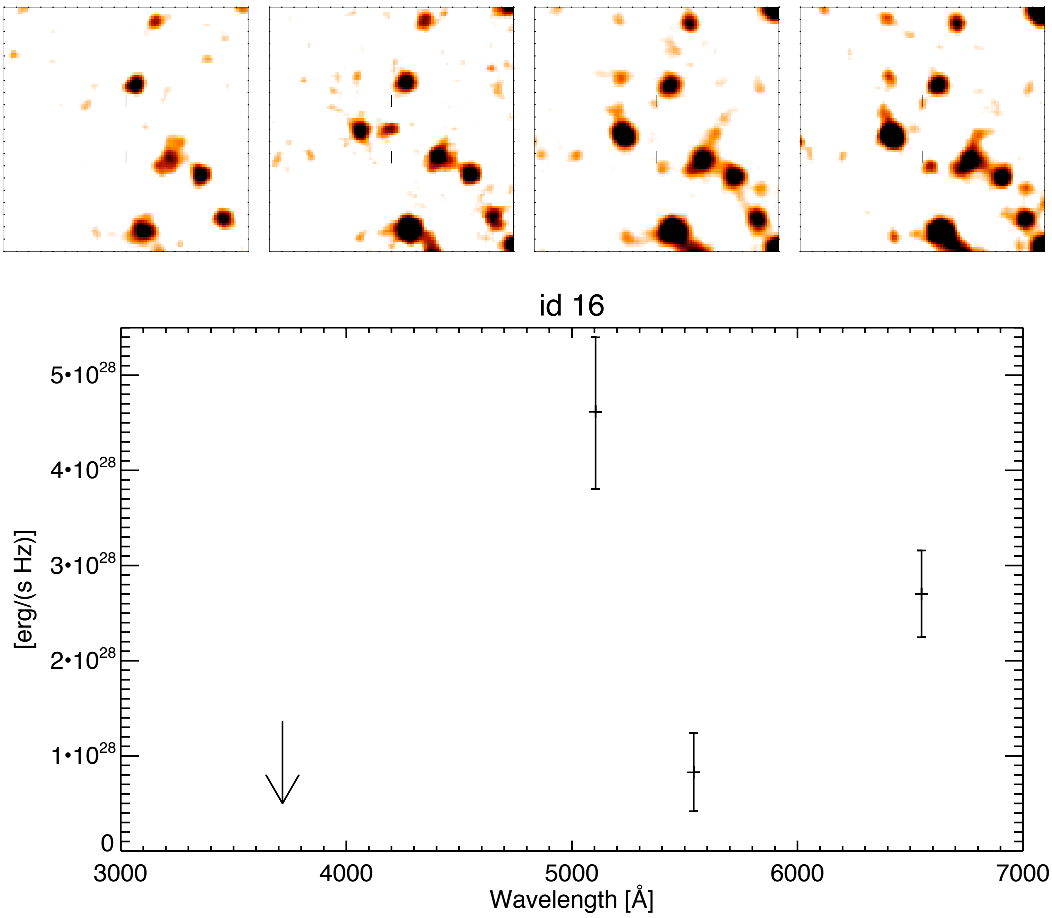

Figure 4.16: 17×17 arcsec^2 images and SED of LAE-id16. Upper part of this figure shows four stamp images of the LAE. From left to right, the four images is in the respective filter-bands: NB_{LyC}, $NB_{\mathrm{Ly}\alpha}$, V and R. The position of the LAE is marked on each image. Lower part of this figure is the SED from the numbers in table 4.2 and the central or effective wavelength of the respective filter-bands.

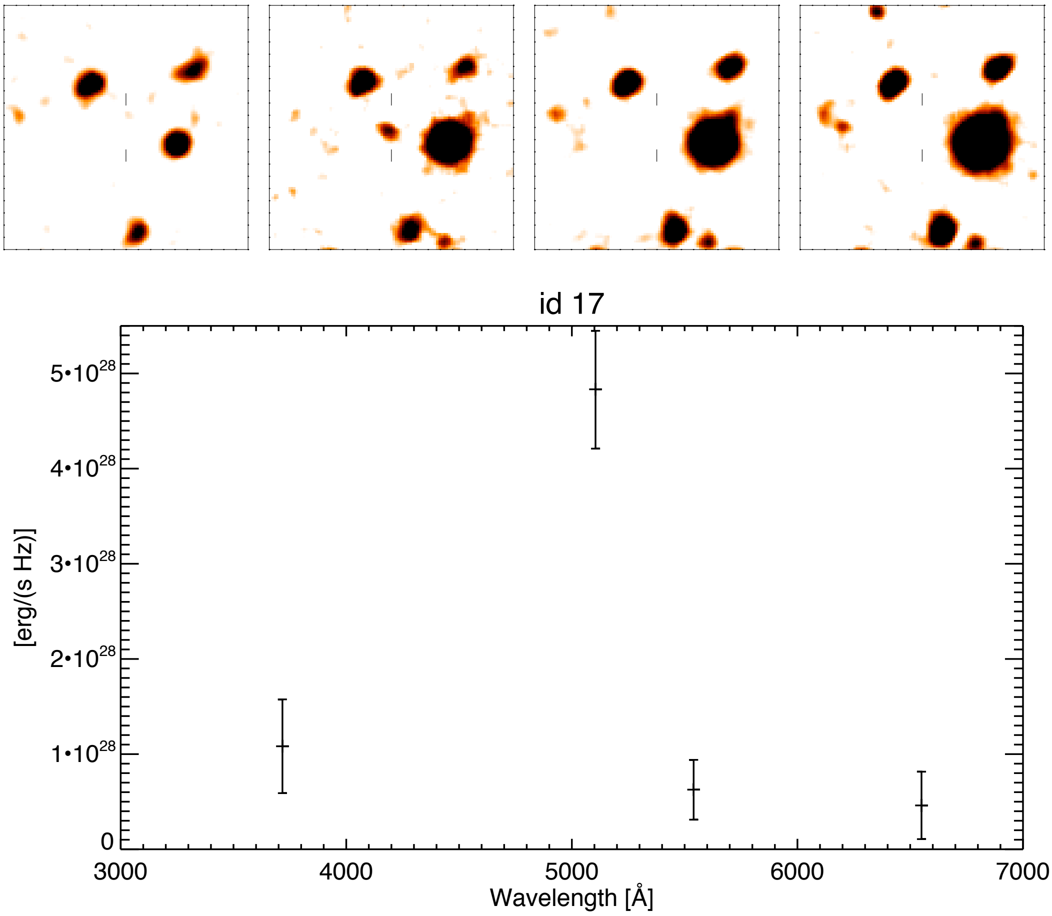

Figure 4.17: 17×17 arcsec^2 images and SED of LAE-id17. Upper part of this figure shows four stamp images of the LAE. From left to right, the four images is in the respective filter-bands: $NB_{\rm LyC}$, $NB_{\rm Ly\alpha}$, V and R. The position of the LAE is marked on each image. Lower part of this figure is the SED from the numbers in table 4.2 and the central or effective wavelength of the respective filter-bands.

4.3 The Escape Fraction of Ionizing Photons

Now, we are finally ready to calculate the LyC escape fractions of the LAEs. I will only estimate the escape fractions for those LAEs in my sample which are detected in the R band image. The reason for this is that I use this filter as comparison with NB_{LyC} filter. The LAE which are detected in LyC (LAE-id02, LAE-id07, LAE-id08) are all detected in the R band filter. Their are 9 more objects which are detected in the R filter, I will put upper boundaries for escape fraction on them. Let us start with defining more precisely want we mean, when we talk about the escape fraction, f_{esc}. I use the same definition and approach as Inoue et al. (2005).

We can define one type of escape fraction, also called the absolute escape fraction as:

$$f_{\mathrm{esc}} \equiv \frac{L_{\mathrm{LyC}}^{\mathrm{out}}}{L_{\mathrm{LyC}}^{\mathrm{int}}} = \exp\Big(-\tau_{\mathrm{LyC}}^{\mathrm{ISM}}\Big) \tag{4.4}$$

where $L_{\mathrm{LyC}}^{\mathrm{int}}$ is the intrinsic LyC luminosity density in units of erg s^{-1}Hz^{-1}. This is a measure of how many ionizing photons that is present inside the LAE. $L_{\mathrm{LyC}}^{\mathrm{out}}$ is the LyC luminosity density just outside the LAE. Assuming that all the LyC photons just outside the LAE originate from the same LAE, the fraction of these two numbers is the escape fraction f_{esc}. It is also a measure of the LyC opacity $\tau_{\mathrm{LyC}}^{\mathrm{ISM}}$, of the interstellar medium (ISM) inside the LAE. We can also define another type, called the relative escape fraction $f_{\mathrm{esc,rel}}$. We use (4.4) in the definition of $f_{\mathrm{esc,rel}}$:

$$f_{\mathrm{esc,rel}} \equiv f_{\mathrm{esc}}\Big(\frac{L_{\mathrm{UV}}^{\mathrm{out}}}{L_{\mathrm{UV}}^{\mathrm{int}}}\Big)^{-1} = f_{\mathrm{esc}}\exp\Big(\tau_{\mathrm{UV}}^{\mathrm{ISM}}\Big) \tag{4.5}$$

the $L_{\mathrm{UV}}^{\mathrm{int}}$ and $L_{\mathrm{UV}}^{\mathrm{out}}$ are respectively the intrinsic luminosity and the luminosity just outside the LAE of non-ionizing UV photons. $\tau_{\mathrm{UV}}^{\mathrm{ISM}}$ is the opacity of the non-ionizing photons.

It is customary in the literature to use the relative escape fraction $f_{\mathrm{esc,rel}}$. The reason for this is that we can rewrite (4.5) as 3 different factors, which we are able measure or model. To do this, we will have to take the IGM opacity into account. This is important for emission below the Lyα -line at 1216 Å in the rest-frame. We introduce the observed luminosity: $L_{\lambda}^{\mathrm{obs}} = L_{\lambda}^{\mathrm{out}}\exp\big(-\tau_{\lambda}^{\mathrm{IGM}}\big)$ for the rest-frame wavelength $\lambda < 1216$ Å, and we assume that $L_{\lambda}^{\mathrm{obs}} = L_{\lambda}^{\mathrm{out}}$ for wavelength $\lambda > 1216$ Å. That is to say, we are assuming that the IGM dust extinction is negligible. In the literature it is common to use 1500 Å as the non-ionizing reference, I will do the same. We can now rewrite (4.5) by inserting (4.4) into (4.5) and use the IGM

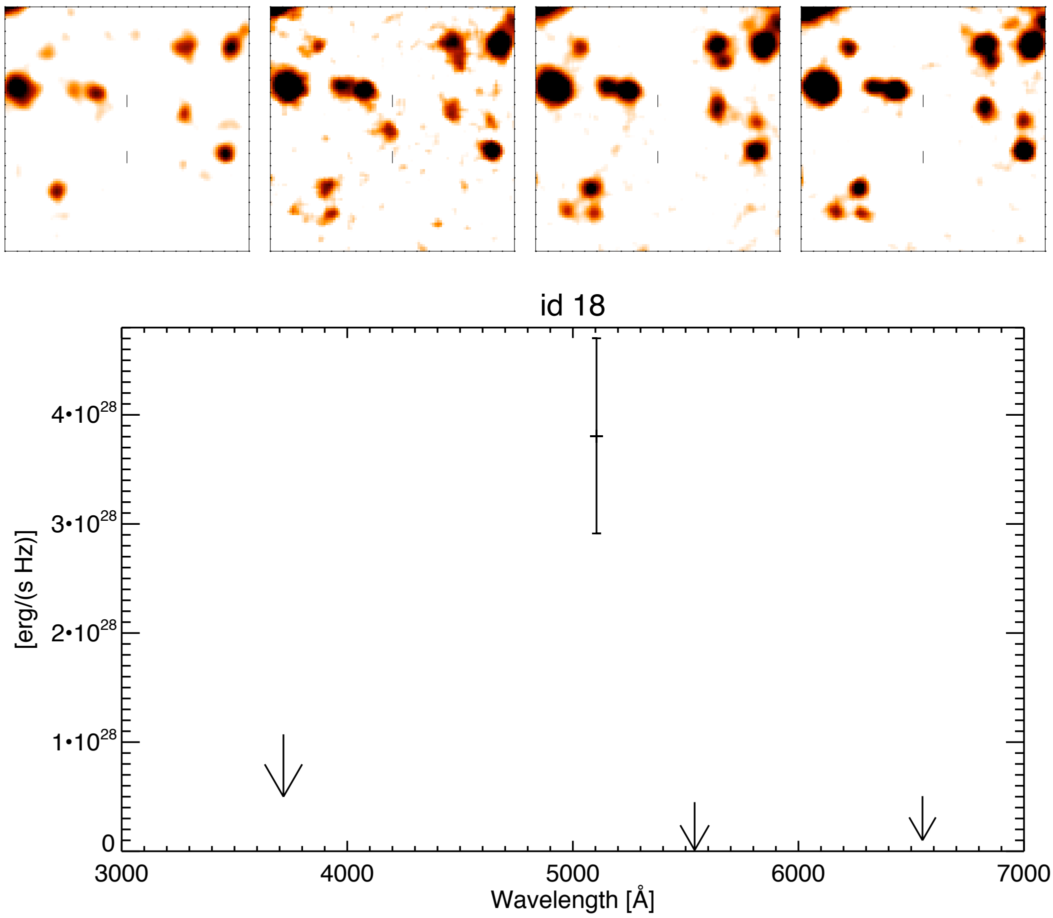

Figure 4.18: 17×17 arcsec^2 images and SED of LAE-id18. Upper part of this figure shows four stamp images of the LAE. From left to right, the four images is in the respective filter-bands: NB_{LyC}, $NB_{\mathrm{Ly}\alpha}$, V and R. The position of the LAE is marked on each image. Lower part of this figure is the SED from the numbers in table 4.2 and the central or effective wavelength of the respective filter-bands.

opacity:

$$
\begin{aligned}
f_{\mathrm{esc,rel}} &= f_{\mathrm{esc}} \left(\frac{L_{\mathrm{UV}}^{\mathrm{out}}}{L_{\mathrm{UV}}^{\mathrm{int}}} \right)^{-1} \\
&= \left(\frac{L_{\mathrm{UV}}}{L_{\mathrm{LyC}}} \right)_{\mathrm{int}} \times \left(\frac{L_{\mathrm{LyC}}}{L_{\mathrm{UV}}} \right)_{\mathrm{out}} \\
&= \left(\frac{L_{\mathrm{UV}}}{L_{\mathrm{LyC}}} \right)_{\mathrm{int}} \times \left(\frac{L_{\mathrm{LyC}}}{L_{\mathrm{UV}}} \right)_{\mathrm{obs}} \times \exp\left(\tau_{\mathrm{LyC}}^{\mathrm{IGM}} \right) \\
&= \frac{(L_{\mathrm{UV}}/L_{\mathrm{LyC}})_{\mathrm{int}}}{(L_{\mathrm{UV}}/L_{\mathrm{LyC}})_{\mathrm{obs}}} \exp\left(\tau_{\mathrm{LyC}}^{\mathrm{IGM}} \right) \qquad (4.6)
\end{aligned}
$$

So we can find $f_{\mathrm{esc,rel}}$, from the observed UV-to-LyC luminosity density ratio, if we know the intrinsic UV-to-LyC luminosity density ratio and the IGM opacity.

4.3.1 The Intrinsic Luminosity Density Ratio

We have to use a model, like the Statburst 99 code to estimate the UV-to-LyC luminosity density ratio because this ratio is not well constrained observationally, as noted by Steidel et al. (2001). However, modeling this intrinsic ratio will also lead to a range of values, *e.g.* Inoue et al. (2005) find $L_{1500}/L_{900} = 1.5 - 5.5$ using the Starburst 99 model, assuming a constant star formation rate, the Salpeter initial mass function with the mass range of $0.1 - 100 M_{\odot}$, and the matallicity of $0.001 - 0.02$, where 0.02 is the solar value. In the literature it is common practise to use $L_{1500}/L_{900} = 3$, when comparing the intrinsic luminosity densities at 900 Å and 1500 Å, see *e.g.* Steidel et al. (2001), Inoue et al. (2005), Shapley et al. (2006) and Iwata et al. (2009). Since I am going to use the R band which has an effective wavelength of 6550 Å corresponding to a wavelength of 1560 Å in rest-frame I will do the same, and choose the value of 3 for the UV-to-LyC luminosity density ratio.

4.3.2 The Intergalactic Medium Opacity

Since the LyC photons can be absorbed by Lyα absorption in HI clouds, an average opacity of the IGM can be estimated from the number distribution functions of the Lyα forest and denser clouds, see *e.g.* Madau (1995). I am using a small IDL code called Lyman_blanket.pro based on the model by Madau (1995). I am using the LAE redshifts reported by Grove et al. (2009) as input to the code as well as the observed wavelength of 3717 Å of the LyC. I find averaged opacities in the range $\tau_{\mathrm{LyC}}^{\mathrm{IGM}} = 1.73 - 1.96$.

4.3.3 Results

We can now calculate the relative escape fractions $f_{\mathrm{esc,rel}}$ using (4.6). I estimate the uncertainty of the escape fractions, assuming that their are no uncertainties in $\tau_{\mathrm{LyC}}^{\mathrm{IGM}}$

id	z	$(L_{\mathrm{UV}}/L_{\mathrm{LyC}})_{\mathrm{obs}}$	$\exp(\tau_{\mathrm{LyC}}^{\mathrm{IGM}})$	$f_{\mathrm{esc,rel}}$
1	3.2161	8.09064	6.84538	< 2.54
2	3.2012	7.53840	6.29957	2.51 ± 0.38
3	3.1804	0.664400	5.61643	< 25.36
4	3.1804	5.90142	5.66906	< 2.88
5	3.2070	3.15920	6.50610	< 6.18
7	3.2087	0.885517	6.56806	22.25 ± 6.03
8	3.2222	1.49321	7.08376	14.23 ± 5.51
9	3.2106	14.0897	6.63803	< 1.41
10	3.2106	0.798808	6.23002	< 23.40
12	3.1862	0.450945	5.79828	< 38.57
16	3.1978	1.97664	6.18185	< 9.38
17	3.2057	0.425601	6.45916	< 45.53

Table 4.3: The estimated relative escape fraction and the numbers that are used to determine the relative escape fraction

and the intrinsic UV-to-LyC luminosity density ratio. The result are presented in table 4.3 together with $(L_{\mathrm{UV}}/L_{\mathrm{LyC}})_{\mathrm{obs}}$ and $\exp(\tau_{\mathrm{LyC}}^{\mathrm{IGM}})$. The redshifts in the table are taken from Grove et al. (2009). The numbers I find are unrealistically high and I will discuss this in the next chapter.

Chapter 5

Summary and Discussion

In this final chapter, I will give a summary of my work and of the results of the measurements. I will also discuss the implication of my findings and compare them with previous works by others.

5.1 Summary

I have calibrated, stacked and combined a total number of 54 science images of the field of BRI1202-0725, with a total integration time of 28.4 hr. This field have 18 spectroscopically confirmed LAEs at redshift $z \sim 3.2$. The data I have worked on is obtain using an OII-filter in front of the FORS1 instrument mounted at the VLT. This OII-filter probes the LyC emission of the LAEs, just below the Lyman-limit in the rest-frame of the LAEs. Out of these 18 LAEs, I detect a flux above a 3σ detection-limit in 3 cases. For these 3 cases I find the detection confidence to be: LAE-id2 $\sim 6.7\sigma$, LAE-id7 $\sim 5.2\sigma$ and LAE-id8 $\sim 3.2\sigma$. However, for LAE-id2 the flux seem to come from a close neighboring object, and not from the LAE itself. For the two other cases the flux do seem to come from the LAEs, although it originate from only a small area compared to the spatially extended area of Lyα emission.

Beside the OII-filter data, I have the magnitudes of my sample LAEs in the 3 wavelength bands OIII, V and R . I have this data from Grove et al. (2009). Using this data I have calculated the luminosity density in all 4 wavelength bands and constructed a SED for all 18 LAEs. In my sample of 18 LAEs, their is 12 which are detected in the R filter. For these LAEs I can compare the luminosity density of the 12 LAEs in the R - and OII-filter. This, I use to estimate the relative escape fraction of LyC photons. This number, estimates the number of ionizing photons relative to the number of non-ionizing UV photons that leaves the star-forming galaxies. The number is important to know the estimated size of, in order to determent how much star-forming galaxies contributes to the ionization of the Universe. The numbers I find for the my sample of LAEs are in no agrement with what is published for LBGs in the literature.

5.2 Discussion

The object LAE-id2 is the most luminous object in my sample. It is also the object with the most secure detection of flux ($\sim 6.7\sigma$) in the filter that probes the LyC. This gives the LAE-id2 an measured AB magnitude of $25.73^{+0.18}_{-0.15}$ in the OII-filter band. However, by visual inspection of the small stamp image in figure 4.3, I argue that the majority of the measured flux originate from the possible foreground galaxy close to the line-of-sight to the LAE. The foreground galaxy is to the upper right of LAE-id2. I do not consider this to be a detection of LyC emission from a star-forming galaxy. However, it might be that we are measuring some LyC emission from this source, if we do, it is buried in the much stronger foreground source.

This leaves me with the two detections LAE-id7 and LAE-id8. I do consider these detections to be very likely LyC emission from star-forming galaxies. By inspection of the stamp images, it seem that the emission in the OII-filter band originate from inside the area of the Lyα emission in the OIII-filter band. This difference in size and shape of flux area detected in LyC compared to the one detected in Lyα is in agrement with what Iwata et al. (2009) finds. As noted by Iwata et al. (2009), this can be explained by the assumption, that the LyC escapes through a chimney like structure in the interstellar medium (Razoumov and Sommer-Larsen, 2007). Another explanation could be that the spatial distribution of the young massive stars that creates the LyC photons, is not uniform throughout the individual galaxies.

Both LAE-id7 and LAE-id8 are detected in all four wavelength bands and they seem to have a flat continuum at the same level on both side of the Lyα emission-line, as estimated by inspection of the SED. As a consequence of the flat continuum, these two detected objects have very blue color: $NB_{\mathrm{LyC}} - R = -0.13$ for LAE-id7 and $NB_{\mathrm{LyC}} - R = 0.44$ for LAE-id8. Other LAEs in my sample are also very blue. However, that can generally be explained by the fact that they are not detected in the OII-filter band or R -filter band or both. The blue colors of my two detected LAEs are consistent with what Iwata et al. (2009) finds for their detected LAEs. They state that they can find similar blue colors using a Population III model by Schaerer (2003), but as they also mention, it is hard to believe the existent of Population III stars at redshift $z \sim 3.2$.

I am estimating the relative escape fractions for those objects that have been detected in the R band. For those which are not detected, in the OII band, I can only put an upper limit on $f_{\mathrm{esc,rel}}$. However, the numbers I find are ridiculously high. It is not so much that my calculations give more than 100%, that could in principle be true, because it is the number of ionizing photons *relative* to the number of non-ionizing photons that escapes the galaxy. Even though it is more believable with $f_{\mathrm{esc,rel}}$ less than 100%. The problem is that these numbers are so much higher than what reasonable can be expected, maybe a factor of a hundred or so. And without doubt much higher than published by others in the literature for LBGs. I have check my zero point measurement and calculation carefully, but I have not been able find any mistakes at the time of writing. However, the conversion factor from one aperture to another, changes from one star to another. It changes from ~ 1.2 to ~ 1.6, and the value of 1.36 I use, is the conversion factor I found from measuring the star I used to find the zero point with - and it lies in between the two other values. This should not mean so much since I am taken the logarithm of the number and it does not explain the very large numbers I find. I have also checked my calculations from magnitudes to escape fractions more than one time, and I have not been able find any mistakes their either. I will therefor assume that my calculations and measurements are correct.

One assumption that is needed to find $f_{\rm esc,rel}$ is that the intrinsic luminosity density ratio of non-ionizing radiation to the ionizing radiation is 3. However, Iwata et al. (2009) find for their bluest model galaxies generated with the Starburst 99 code, that this value should be 1.07. If I use this value it will improve my $f_{\rm esc,rel}$ with a factor of ~ 3. Not much, but a step in the right direction. Using the Lyman_blanket code based on the model by Madau (1995), I find $\tau_{\rm LyC}^{\rm IGM} = 1.73 - 1.96$. These values seem to be a little on the high side at $z \sim 3.2$ compared to *e.g.* Steidel et al. (2001), Inoue et al. (2005), Shapley et al. (2006) and Iwata et al. (2009). This could give me another factor of two. However, non of these adjustments will bring my numbers near anything that seem realistic.

Another possibility is that my sample is contaminated with low redshift galaxies. The followup spectroscopy done by Grove et al. (2009), should in principle sort the sample by the confirmation of and emission line at the right place in the spectra of the LAE. And the absence of other emission lines at longer wavelengths should exclude any low redshift emission line galaxy. However, this method is not 100% bulletproof.

Iwata et al. (2009) detect LyC emission from 7 LBGs and 10 LAEs. It is unfortunate that they do not publish any calculation of the escape fraction of the LAEs in their sample, only the numbers from the LBGs are published. I find the same blue colors of my two detected LAEs as they do. Could it be that they find the same ridiculously high numbers I do, and choose not to publish, because they can not understand these numbers? This is of cause only a guess. However, if my calculations are right, it seems that we can not use the same assumptions when we find escape fractions for LAEs as we use when find escape fractions for LBGs. We simply need to better under what LAEs are before we can find meaningful escape fraction from this type of star-forming galaxies. The ultimate goal must be to find relations between the escape fractions of LBGs and LAEs, and other properties of these star-forming galaxies, like their star-formation rate and colors. Only then, can we hope to say something general about the contribution of these star-forming galaxies to the intergalactic ionizing UV background.

Although I did not succeed in finding meaningful escape fractions, I do detect LyC emission from 2 out of 18 LAEs, so it seem that narrow-band imaging is useful when we want to look for ionizing emission from star-forming galaxies.

Appendix A

Charged-Coupled Device

Today the most common way of collecting astronomical data is by using a charged-coupled device (CCD) chip placed at the focal plane of the telescope. It was a huges breakthrough for observational astronomy when the CCD chip replaced the old photographic plates as the preferred tool for collecting data in the UV, visual and IR wavelength band. This is because the data from the CCD can be stored and analyzed directly on a computer and the light efficiency of the CCD is much greater than the old photographic plates.
The surface of a CCD chip is divided into rows and columns of pixels. The physical size of each pixel is 10 - 20 μm. The typical number of pixels in a modern CCD are 4 mega pixel or more and often two or more CCD's are placed next to each other so the resulting astronomical image of the sky consist of a mosaic of images, one from each CCD in the focal plane. This gives a better spatial resolution of sky.
The CCD is constructed by doping a ~ 260 μm silicon substrate with phosphorus so it become a p-type semiconductor. If the CCD is specially constructed to be sensitive in the blue wavelength area the p-type substrate will be made thinner because the CCD is lite from the bottom (Sparke and Gallagher, 2000). On top of this silicon substrate another very thin ($\sim$ 2 μm) silicon substrate doped with e.g. boron is placed. When this n-type semiconductor comes into contact with the p-type, the free electrons in the n-type semiconductor is moving into the upper part of the p-type semiconductor and fils the positive holes there. This creates a ~ 10 μm upper region of the silicon substrate that is depleted of free charges and hence has very little conductivity. This region can support an electric field that is directed downward due the proximity of the strong positive charge in the n-type semiconductor region. Above the silicon substrate, electrodes in a thin insulating layer of SiO_2 are placed. The electrodes has no direct contact to the n-type semiconductor layer. Each pixel have three electrodes on top.
When the CCD is exposed to light photons will be absorbed in the silicon layers. Because of the photoelectric effect, an electron from the silicon lattice can be ejected and find it self in a state known as the conducting band an leave a "hole" in the lattice. Not all incoming photons will produce an electron-hole pair, the ratio of

ejected electrons to the number of incoming photons is called the *quantum efficiency* (QE) and for modern CCD's it is around $80 - 90\%$ depending on the energy of the photon. Electron-hole pair created in the depleted silicon substrate will feel the presence of the electric field and the electrons will start to move up into the n-type substrate. The "number 1" electrode in each pixel is kept at a relative high positive potential which causes the electrons to collected under this particular electrode, but still in the n-type layer. During an exposure more and more electrons will move up an accumulate under the "number 1" electrode. After the exposure the information has to be read out and stored on a computer. By changing the voltage on the three different electrodes in each pixel, the accumulated electrons are shifted from electrode 1 to 2 and 3 and then onto the electrode 1 on the next pixel, e.g. from left to right. The electrons in the right most column are moved out of the detector array and into a transfer register from were the sequence of charges is captured and amplified by a field-effect transistor. This analog signal is then fed into an analog-to-digital converter which convert the signal into a digital image that can be stored an manipulated on a computer.
A number of things can generate noise, either during the exposure or after when the CCD is being read out. The most important sources of noise experienced are:

Read-out noise (RON) When the analog signal is converted into a digital image, noise is introduced into the signal because of the random component of the conversion. This means, that if you read out the same pixel twice and it has accumulated the same number of charges it will in general still not be converted to the same digital output number.

Dark current This is caused by spontaneous excitations of electrons that can be collected under a electrode. This will of cause add to the total number of electrons collected in that pixel. The dark current can be reduced, or practically eliminated by cooling the CCD chip to $\sim$ 173 K, and when using modern telescopes the dark current is of no real consequence. If one is using a CCD without the proper cooling, it is possible to subtract the dark current from the science image. This done by taken "dark images" with the same exposure time as the science images, but with the CCD shutter. closed.

Shot-noise The arrival of photons is a random and discrete process also called a stochastically process. Because the arrival of each photon is an independent event that cannot be predicted, the probability of a photon arriving at any given time is governed by a Poisson distribution. Shot-noise is most apparent when collecting a relatively small number of photons. It can be reduced by collecting more photons, either with a longer exposure or by combining multiple frames.

Electro-Magnetic Interference The detector signal may be influenced by the presence of electro-magnetic waves from nearby electronics. This can show up as a fishbone pattern in the image. The best way to eliminate this noise source, is to the CCD in such a way that the chip is shielded in best possible way from EMI.

Cosmic Energetic particles hitting the detector may interact and leave a trail of electron-hole pairs in one or more pixels. These events are generally called cosmic, although the particles often are not cosmic in origin. Cosmic will often showup as spikes on the images. The rate of these events are typically $1 - 2\frac{\mathrm{hits}}{\mathrm{cm}^2\mathrm{minute}}$ and is mainly a problem for long exposures. It is possible to eliminate most cosmic by combining multiple frames.

overscan When we readout the CCD it is customary to keep reading out beyond the physical size of CCD. This will create an overscan region. The overscan region is an estimate of the zero offset on "empty" pixels *i.e.*, it provides a measure of the electronics bias level that physically indicates zero photons counted (Gilliland, 1992). We correct for this by takeing the median of a portion of the overscan region and subtract it from every images, flat or bias we take.

Bias A CCD will in general have electronic zero point pattern that is repeated for each CCD readout. WE can correct for this by takeing a number of bias-frames, which is turn into a master-bias by takeing the median of set of raw bias. The master-bias is then subtracted form the science and flats.

Gain (flat-field) The different pixels on the CCD chip has different QE and the optics may not illuminate the chip uniformly. The consequence of this is that one will have to correct for these variations by takeing a number of flats and then produce a master flat. The master flat often made taken the median of the raw flats. The master flat is then normalized before one subtract it from the science image. The best flats is usually sky-flats, images of the uniformly light sky just before sun set or sun rise. Flats is one of most important corrections to made when reducing science image.

For more on subject of CCD noise sources and reduction processes, see Gilliland (1992).

Appendix B

Tables

B.1

Year	dates	Number of raw bias	Chip number	Master bias (output)
2005	05-12	5	-	BIAS_2005-05-13.fits
2005	07-02	5	-	BIAS_2005-07-02.fits
2006	04-24 05-25 05-26 06-19 06-20 06-28 06-29 07-18 07-19 07-20 07-21	13	-	BIAS_2006_all.fits
2007	04-14	5	1	BIAS_2007-04-14_CHIP1.fits
2007	04-14	5	2	BIAS_2007-04-14_CHIP2.fits
2007	04-18	5	1	BIAS_2007-04-18_CHIP1.fits
2007	04-18	5	2	BIAS_2007-04-18_CHIP2.fits
2007	04-23	5	1	BIAS_2007-04-23_CHIP1.fits
2007	04-23	5	2	BIAS_2007-04-23_CHIP2.fits
2007	05-11	5	1	BIAS_2007-05-11_CHIP1.fits
2007	05-11	5	2	BIAS_2007-05-11_CHIP2.fits
2007	07-11	5	1	BIAS_2007-07-11_CHIP1.fits
2007	07-11	5	2	BIAS_2007-07-11_CHIP2.fits
2008	02-15	5	1	BIAS_2008-02-15_CHIP1.fits
2008	02-15	5	2	BIAS_2008-02-15_CHIP2.fits
2008	03-02	5	1	BIAS_2008-03-02_CHIP1.fits
2008	03-02	5	2	BIAS_2008-03-02_CHIP2.fits
2008	03-05	5	1	BIAS_2008-03-05_CHIP1.fits
2008	03-05	5	2	BIAS_2008-03-05_CHIP2.fits

B.2

Year	Dates	Number of raw flats	Chip number	Master bias used	Master flat (output)
2005	05-13	4	-	BIAS_2005-05-13.fits	Flat_2005-05-13.fits
2005	07-02	4	-	BIAS_2005-07-02.fits	Flat_2005-07-02.fits
2006	04-24 05-24 05-25 06-29 07-18	5	-	BIAS_2006_all.fits	Flat_2006_all.fits
2007	04-22	4	1	BIAS_2007-04-23_CHIP1.fits	Flat_2007-04-22_CHIP1.fits
2007	04-22	4	2	BIAS_2007-04-23_CHIP2.fits	Flat_2007-04-22_CHIP2.fits
2007	05-10	4	1	BIAS_2007-05-11_CHIP1.fits	Flat_2007-05-10_CHIP1.fits
2007	05-10	4	2	BIAS_2007-05-11_CHIP2.fits	Flat_2007-05-10_CHIP2.fits
2007	07-11	4	1	BIAS_2007-07-11_CHIP1.fits	Flat_2007-07-11_CHIP1.fits
2007	07-11	4	2	BIAS_2007-07-11_CHIP2.fits	Flat_2007-07-11_CHIP2.fits
2008	02-16	4	1	BIAS_2008-02-15_CHIP1.fits	Flat_2008-02-16_CHIP1.fits
2008	02-16	4	2	BIAS_2008-02-15_CHIP2.fits	Flat_2008-02-16_CHIP2.fits
2008	03-02	4	1	BIAS_2008-03-02_CHIP1.fits	Flat_2008-03-02_CHIP1.fits
2008	03-02	4	2	BIAS_2008-03-02_CHIP2.fits	Flat_2008-03-02_CHIP2.fits
2008	03-05	4	1	BIAS_2008-03-05_CHIP1.fits	Flat_2008-03-05_CHIP1.fits
2008	03-05	4	2	BIAS_2008-03-05_CHIP2.fits	Flat_2008-03-05_CHIP2.fits

Bibliography

S. Bajtlik, R. C. Duncan, and J. P. Ostriker. Quasar ionization of lyman-α clouds. *The Astrophysical Journal*, 327:570–583, 1988.

R. H. Becker, X. Fan, R. L. White, M. A. Strauss, and V. K. Narayanan. Evidence for reionization at $z \sim 6$: Detection of a gunn-peterson though in a $z = 6.28$ quasar. *The AStronomical Journal*, 122:2850–2857, 2001.

Stuart Bowyer, Eric J. Korpela, Jerry Edelstein, Michael Lampton, C. Morales, J. Pérez-Mercader, J. F. Gómez, and J. Trapero. Eurd data provide strong evidence against the sciama model of radiative decay of massive neutrinos. *AStrophysics and Space Science*, 276:15–161, 2001.

A. Dall'Aglio, L. Wisotzki, and G. Worseck. The uv background photoionization rate at $2.3 \leq z \leq 4.6$ as measured from the sloan digital sky survey. arXiv:0906.1484, 2009.

X. Fan, C. L. Carilli, and B. Keating. Observational constraints on cosmic reionzation. *Annu. Rev. Astro. Astrophys.*, (44):415–462, 2006.

A. Fernández-Soto, K. M. Lanzetta, and H.-W. Chen. *Mon. Not. R. Astron. Soc.*, 342, 2003.

S. R. Furlanetto, A. Sokasian, and L. Hernquist. Observing the reionization epoch through 21-centimetre radiation. *Mon. Not. R. Astron. Soc.*, 347:187–195, 2004.

J. P. U. Fynbo, C. Ledoux, P. Møller, B. Thomsen, and I. Burud. The building the bridge survay for $z = 3$ lyα emitting galaxies. *AA*, 407:147–157, 2003.

E. Giallongo, S. Cristiani, S. D'Odprico, and A. Fontana. *Astrophysical journal*, 568, 2002.

Ronald L. Gilliland. Details of noise sources and reduction processes. *ASP Conference Series*, 23:68–89, 1992.

L. F. Grove, J. P. U. Fynbo, C. Ledoux, M. Limousin, P. Møller, K. Nilsson, and B. Thomsen. The building the bridge survey for $z = 3$ lyα emitting galaxies. ii. completion of the survey. *AA*, 2009.

J. E. Gunn and B. A. Peterson. On the of neutral hydrogen in intergalactic space. *Astrophysical Journal*, 142:1633–1636, 1965.

M. Hamuy, N. B. Suntzeff, S. R. Heathcote, A. R. Walker, P. Gigoux, and M. M. Phillips. Spectrophotometric standard stars. *Publications of the Astronomical Society of the Pacific*, 106(566), 1994.

A. K. Inoue, I. Iwata, J.-M. Deharveng, V. Buat, and D. Burgarella. Vlt narrow-band photometry in the lyman continuum of two galaxies at $z \sim 3$. *Astronomy & Astrophysics*, 435:471–482, 2005.

Akio K. Inoue and Ikuru Iwata. A monte carlo simulation of the intergalactic absorption aand the detectability of the lyman continuum from distant galaxies. *Mon. Not. R. Astron. Soc.*, 2006.

I. Iwata, A. K. Inoue, Y. Matsuda, H. Furusawa T. Hayashino, K. Kousai, M. Akiyama, T. Yamada, D. Burgarella, and J.-M. Deharveng. Detections of lyman continuum from star-forming galaxies at $z \sim 3$ through subaru/suprime-cam narrow-band imaging. *The Astrophysical Journal*, 692:1287–1293, 2009.

Malcolm S. Longair. *Galaxy Formation*. Springer, 2. edition, 2008.

Piero Madau. Radiative transfer in a clumpy universe: The colors of high-redshift galaxies. *The Astrophysical Journal*, 441:18–27, 1995.

Piero Madau, Franceso Haardt, and Martin J. Rees. Radiation transfer in a clumpy universe. iii. the nature of cosmological ionizing sources. *The Astrophysical Journal*, 514:648–659, 1999.

P. Møller and P. Jakobsen. *Astronomy & Astrophysics*, 228, 1990.

P. Møller and S. J. Warren. Emssion from damped Lyα absorber at $z = 2.81$. *Astron. AStrophys.*, 270:43–52, 1993.

K. K. Nilsson, J. P. U. Fynbo, P. Møller, J. Sommer-Larsen, and C. Ledoux. A lyman-α blob in the goods south field: evidence for cold accretion onto a dark matter halo. *Astronomy & Astrophysics Letters*, 452:23–26, 2006.

J. B. Oke. Absolute spectral energy distributions for white dwarfs. *Astrophysical Journal Supplement Series*, 27(236):21–25, 1974.

J. B. Oke. Faint spectrophotometric standard stars. *The Astronomical Journal*, 99 (5):1621–1631, May 1990.

L. Page, G. Hinshaw, E. Komatsu, M. R. Nolta, D. N. Spergel, C. L. Bennet, C. Barnes, R. Bean, O. Doré, J. Dunkley, M. Halpern, R. S. Hill, N. Jarosik, and A. Kogut. Three-year wilkinson microwave anisotropy probe (wmap) observation: Polarization analysis. *The Astrophysical Journal Supplement Series*, 170: 335–376, June 2007.

A. O. Razoumov and J. Sommer-Larsen. Modeling lyman continuum emission from young galaxies. *Astrophysical Journal*, 668:674–681, 2007.

Barbara Ryden. *Introduction to Cosmology*. Pearson, 2003.

D. Schaerer. The transition from population iii to normal galaxies. *Astronomy and Astrophysics*, 397:527–538, 2003.

D. W. Sciama. Updataed parameters for the decaying neutrino thoery and eurd opservations of the diffuse uv background. *Astron. Astrophys.*, 335:12–18, 1998.

A. E. Shapley, C. C. Steidel, M. Pettini, and K. L. Adelberger D. K. Erb. The direct detection of lyman continuum emission from star-forming galaxies at $z \sim 3$. *The Astrophysical Journal*, 651:688–703, 2006.

Antoinette Songaila. The evolution of the intergalctic transmission to redshift 6. *The Astronomical Journal*, 127:2598–2603, 2004.

Linda S. Sparke and John S. Gallagher. *Galaxies in the Universe*. Cambridge University Press, 1. edition, 2000.

Steven W. Stahler and Francesco Palla. *The Formation of Stars*. Wiley-VCH, 1. edition, 2004.

C. C. Steidel, M. Giavalisco, M. Pettini, M. Dickinson, and K. L. Adelberger. *Astrophysical Journal*, 462:17, 1996.

Charles C. Steidel, Max Pettini, and Kurt L. Adelberger. Lyman-continuum emission from galaxies at $z \simeq 3.4$. *The Astrophysical Journal*, 546:665–671, 2001.

L. J. Storrie-Lombardi, M. J. Irwin, and R. G. McMahon. Apm $z \geq 3$ survey: distribution and evolution of high column density hi absorbers. *Mon. Not. R. Astron. Soc.*, 282:1330–1342, 1996.